TECHNICKÁ UNIVERZITA V LIBERCI
Fakulta mechatroniky, informatiky
a mezioborových studií

ADVANCED TIME AVERAGE DIGITAL HOLOGRAPHY BY MEANS OF FREQUENCY AND PHASE MODULATION

PhD dissertation - report

Study program: P3901 Applied Sciences Engineering
Field of study: 3901V055 Applied Sciences Engineering

Author: **Ing. Pavel Psota**
Supervisor: prof. Ing. Václav Kopecký, CSc.
Consultant: Ing. Vít Lédl, Ph.D.

Liberec 2015

Annotation

This dissertation introduces some developments in the field of time average digital holography widely using as a tool for vibration analysis. The work deals with the most significant drawbacks of the method: limited measurement range and quantitative analysis of the measured Bessel fringe patterns. Different frequency modulation of an object wave and a reference wave in experimental arrangements results in temporally harmonic variation of intensity values of a digital hologram. This feature expresses a relative phase difference between the both waves and therefore any of phase-shifting algorithms can be applied in order to directly calculate a complex field in the hologram plane. This leads on the one hand to improvement of lateral resolution within the reconstructed surface of the object. On the other hand the signal-to-noise ratio is increased. When frequency of the reference wave is in addition modulated by an integer multiple of frequency at which the object oscillates, the measurement range of the method can be shifted either to smaller or to larger vibration amplitudes. The threshold of the smallest measurable amplitude is experimentally established to be under 0.1 nm while the largest measured amplitude is about 10 µm. Phase modulation of the reference wave is used to obtain a sequence of phase modulated fringe patterns (reconstructed fields). Such fringe patterns can be combined by means of phase shifting algorithms and amplitudes of vibrations can be straightforwardly computed. This approach calculates the amplitude values independently in every single pixel. The both frequency and phase modulation are realized by proper control of Bragg cells.

Keywords: Vibration analysis, digital holography, time average holography, frequency modulation, phase modulation, very small amplitudes, vibration amplitude distribution

Anotace

Tato práce rozvijí digitálně holografickou metodu časového středování, která patří mezi důležité nástroje v oblasti analýzy vibrací. Vývoj se zaměřuje na největší slabiny této metody, které jsou její omezený měřicí rozsah a kvantifikace amplitud vibrací z rekonstruovaných polí. Rozdílná frekvenční modulace referenční a objektové vlny holografického uspořádání způsobuje harmonicky se vyvíjející interferenční pole digitálního hologramu. Tato časová proměnnost je určena relativní fázovou změnou mezi oběma vlnami. Toho lze využít pro přímý výpočet komplexního pole v rovině hologramu pomocí některého z rodiny „phase-shifting“ algoritmů. Výsledkem je dosažení lepšího prostorového rozlišení uvnitř měřené oblasti a zvýšení poměru signál-šum. Je-li dále referenční vlna modulována frekvencí odpovídající násobku frekvence měřeného objektu, lze posouvat měřicí rozsah metody do hodnot velmi malých i velkých amplitud vibrací. Prahová hodnota měřitelnosti pro malé amplitudy vibrací byla experimentálně stanovena pod 0.1 nm. Na druhé straně lze metodu modifikovat i pro měření amplitud vibrací kolem cca 10 µm. Kromě frekvenční modulace je možné do metody zakomponovat i modulaci fáze jedné z vln holografického uspořádání. Tímto způsobem získáme sekvenci fázově posunutých interferenčních struktur, které lze opět pomocí „phase-shifting“ algoritmů využít pro výpočet rozložení amplitud vibrací nezávisle v každém bodě povrchu. Frekvenční i fázová modulace je realizována pomocí Braggových cel.

Klíčová slova: Analýza vibrací, digitální holografie, holografie časového středování, frekvenční modulace, fázová modulace, velmi malé amplitudy vibrací, rozložení amplitud vibrací.

Contents

Introduction

The measurement of vibrations is an integral task to engineering [1]. Vibration analysis is on one hand used to ascertain the operation of vast spectrum of components, which should oscillate, like loudspeakers, ultrasonic or piezoelectric transducers, etc., and on the other hand to check the behavior of components, which have natural frequencies within the range of operating frequencies in order to prevent of fatigue failure or to detect noise-generating parts or areas. Obviously, contactless measurement methods which do not affect the vibrations itself are demanded. In many practical cases, the knowledge of amplitude of vibrations in a single point of the surface is not sufficient but a distribution of amplitudes over the whole surface can only provide the complete information.

On the market, there is a broad portfolio of vibration measurement devices, which are usually based on the Doppler phenomenon [2]–[5], correlation analysis [2], speckle ESPI (Electronic Speckle Pattern Interferometry) [3], [4], and others. These methods are mostly single-point methods or their measuring capabilities in terms of maximal amplitudes or frequency range are limited. Thus, an extra care must be taken to parameters of a device when choosing one for a certain application. Another suitable tool for analyzing vibrations in the whole surface is holographic interferometry, which moreover has no limit in vibration frequency. Holographic interferometry comprises two basic principles: holography and interferometry.

In 1948 Gabor presented holography as a lensless process for image formation by reconstructed wavefronts [5]. The breakthrough of holography was initiated by the development of the laser providing a powerful source of coherent light. Now there was a working method for recording and reconstruction of complete wavefields with intensity and phase. Besides the impressive display of 3D scenes exhibiting effects like depth and parallax, holography found numerous applications based on its unique features. Perhaps the most important application of holography is in interferometric metrology, started by discovery of holographic interferometry [6], [7]. The early applications ranged from the first measurement of vibration modes [6], [7], over deformation measurement [8], [9], contour measurement[10], [11], to the determination of refractive index changes [12]–[14].

The wet chemical processing of the holographic plates showed their typical drawbacks. The first attempt to capture a hologram by a digital sensor dates back in 1967 when Goodman and Lawrence [15] recorded a wave field with use of a vidicon. The output of the vidicon was sampled in a 256×256 array, and quantized to eight grey levels. This was the very beginning of digital holography [16]. A boom of digital holography came up with the discovery of modern cameras using CCD or CMOS. Recording and numerical reconstruction of digital holograms were introduced by Schnars and Juptner [17]. The most significant impact of digital holography I find in the branch of digital holographic interferometry (DHI) [18]–[20] and digital holographic microscopy (DHM) [21]–[24].

This thesis develops holographic method in the field of vibration analysis. The pioneering work in this manner was done by Powell and Stetson [6], [7] in 1965. They shew, that the image reconstructed by the hologram exhibits a system of interference fringes, which map contours of constant vibration amplitude. The method was named time average holographic interferometry (TAHI), which, in this basic configuration, is suitable for measurement of amplitudes in range of hundreds of nanometers or units of microns. Shortly, in 1967 Goodman [25] followed by important work of Aleksoff [26] made the first steps in extension of time average holographic interferometry measurement range by means of frequency modulation (FM). The detectable smallest amplitude with frequency modulated TAHI (FMTAHI) was estimated by Ueda et al. [27] to be $2.7\times10^{-4}\lambda$.

Similarly to holography itself, time average holography has significantly changed after arrival of the digital era. Picard et al. [28] has simplified the processing of the data by performing time averaged holography with a digital CCD camera. It was a beginning of time average digital holography (TADH). Heterodyne technique realized by acusto-optical modulators was introduced by Clerc et al. [29]. Further, Joud et al. [30] employed acusto-optical modulators in TADH for large amplitudes measurement while author et al. [31] applied frequency modulation by means of Bragg cells for very small amplitudes. Later on the method with ultimate sensitivity was experimentally verified by Ledl et al. [32]. Other configurations with great sensitivity was presented by Verrier [33].

One of the most important tasks in time-average holography (TAHI or TADH) is to qualitatively determine the amplitude distribution from the fringe pattern modulated by Bessel function. Numerical analysis of cosine fringes (exhibiting in other interferometric techniques) allows the determination of interference phases even between the fringe intensity maxima and minima with high accuracy. While a lot effort has been put to automate the evaluation of cosine fringes coming from holographic interferometry, not a great deal has been done to automate Bessel-type fringe interpretation coming from time average technique. The interference phase (directly connected to the required amplitude of vibration) is most often determined by searching for intensity maxima and minima followed by manual fringe counting and interpolation of values between the fringes. Nevertheless, modern digital cameras provide the advantage of very uniform and repeatable response, and they can be considered as a radiometric detector. Capturing of two digital holograms (one in vibrating and one in steady state), a normalized fringe pattern can be calculated and direct inversion of the intensity field to amplitude distribution is possible. Direct inversion approach was applied by Borzsa [34] and the author in [31]. However, due to not monotonous behavior of Bessel function, the procedure cannot still be fully automatic. Vikram [35] and the author [36] have also used recurrence relation of Bessel function in order to calculate the phase from intensities modulated by different orders of Bessel function. Least square solution of overdetermined systems consisting of

differently modulated intensity maps was proposed by author in [37]. However, none of the method is simultaneously full-field, robust, accurate and fully automated.
Stetson and Brohinski [38] placed a PZT mirror in reference arm of the holographic arrangements in order to alter its phase and shift the Bessel fringes similarly to phase stepping in case of cosine fringes. This inspired the author [39] in order to use Bragg cells in experimental arrangements in his invention to modulate the both phase and frequency of the reference wave, which resulted in quantitative measurement of amplitudes of vibrations independently in every single pixel with extended dynamic range. This method simultaneously addresses two main drawbacks of TADH:

- Extension of the measurement range;
- User friendly, fully automated and quick retrieval of amplitudes independently in every single pixel;

without excessive hardware demands. Moreover, together with complete automatic control and data processing, the method introduces a complete solution for full-field, contactless vibration analysis with unique accuracy and lateral resolution.
This thesis describes the physical nature of the method, experimentally verifies the theoretical claims, searches for limits of the method, discusses possible sources of distortions and quantifies them. Last but not least introduces some results of applied engineering tasks like piezoelectric transformer vibration modes visualization [31], [40]–[44] or measurement of glass shell in noise suppression experiment [45]–[49].

Content of the dissertation

The dissertation is organized into four main chapters. The first two chapters can be summed up as a theoretical part, where some basic and generally-known principles are defined for subsequent use in the text. The last two chapters describe author´s selected contributions in the field of TADH.
Chapter 1 presents the physical prerequisites of digital holography, starting with the wave theory of light, describing effects such as interference, polarization, coherence and diffraction.
Chapter 2 presents the techniques of how to record holograms on a digital sensor. In other words it shows how to solve the problem imposed by the limited resolution of these detectors. Then the chapter introduces the reconstruction of the recorded optical wave field by the numerical reconstruction. Finally, the basic principle of vibration analysis by TADH is introduced.
In Chapter 3 the advantages resulting from Bragg cells employment are described and experimentally verified. Namely it is lateral resolution and signal to noise ratio (SNR) improvement, extension of dynamic range and retrieval of vibration amplitudes. Moreover, error and uncertainty analysis is performed.
Chapter 4 is devoted to experimental results of the developed method. Particularly it is mode visualization of ring and disc piezoelectric transformers and measurement of

amplitudes of vibration generated by a glass shell within a noise suppression experimental study.

1 Digital holography

1.1 Fundamentals of digital holography

Holography involves recording and reconstruction of optical waves. Optical wave carries information about its amplitude and phase; however, only the amplitude information can be retrieved by optical detectors (human eye, photographic film, CCD, CMOS, etc.) as detected intensity. Information about phase of the wave is lost during the recording process. Nevertheless, the phase indicates a directionality of optical waves, thus determines the effects like depth and parallax of the observing scene. Due to lack of "phase-sensitive" detectors, it is necessary to code the phase information into the amplitude information, which can be detected.

Such a code is based on combination of the original wave - the object wave U_0 with a known reference wave U_r and recording their interference pattern. The intensity of the sum of the two waves is recorded, forming a transmittance h. The transmittance (called a hologram) is described by the interference formula:

$$h \approx |U_o + U_r|^2 = |U_o|^2 + |U_r|^2 + U_o U_r^* + U_o^* U_r. \qquad (1.1)$$

The hologram h carries coded information about the intensity and phase of the wave U_o, furthermore the hologram h is highly sensitive to the difference between the phases of the two waves. To decode the information from the hologram and reconstruct the object wave, the reference wave U_r must illuminate the hologram. The result is a wave in the hologram plane $z = 0$ with complex amplitude:

$$U = hU_r \approx U_r(I_r + I_0) + I_r U_0 + {U_r}^2 {U_0}^*. \qquad (1.2)$$

The term $I_r U_0$ is the original wave multiplied by the intensity of the reference wave I_r. If I_r is uniform this term constitutes the desired reconstructed wave. The term ${U_r}^2 {U_0}^*$ is a conjugated version of the original wave modulated by ${U_r}^2$ and the term $U_r(I_r + I_0)$ represent the reference wave, modulated by the sum of the intensities of the reference I_r and the object I_0 wave.

The recording and reconstruction procedures are schematized in Figure 1.1. The aim of digital holography is to record holograms, which are later stored in a computer memory and can be reconstructed numerically afterwards. The digital recording medium is usually CCD or CMOS camera. The basic principle of digital hologram recording is the same as in the conventional holography. Only the recording medium is different having worse spatial resolution when compared to classical holographic plate. A meaningful sampling of the intensity distribution constituting the hologram is only guaranteed if

the sampling theorem is followed. The sampling theorem requires that the spatial period Λ must be sampled with more than two pixels:

$$\Lambda > 2\Delta\xi, \tag{1.3}$$

where $\Delta\xi$ is the pixel size. For small values of angle θ we can consider $sin\theta \approx \theta$.

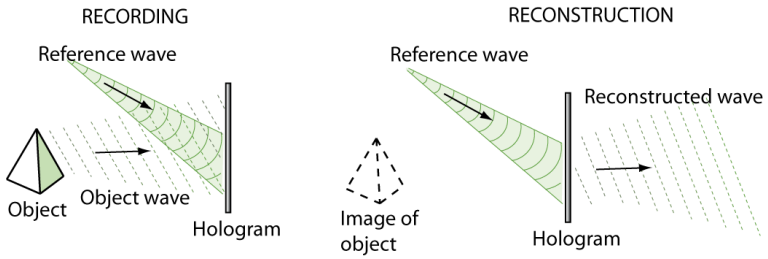

Figure 1.1: Principle scheme of a hologram recording and its reconstruction.

Hence, the limit value for the angle θ_{max}, which is the maximum angle formed by reference and object wave when the sampling theorem is followed, can be determined as:

$$\theta_{max} \approx \frac{\lambda}{2\Delta\xi}. \tag{1.4}$$

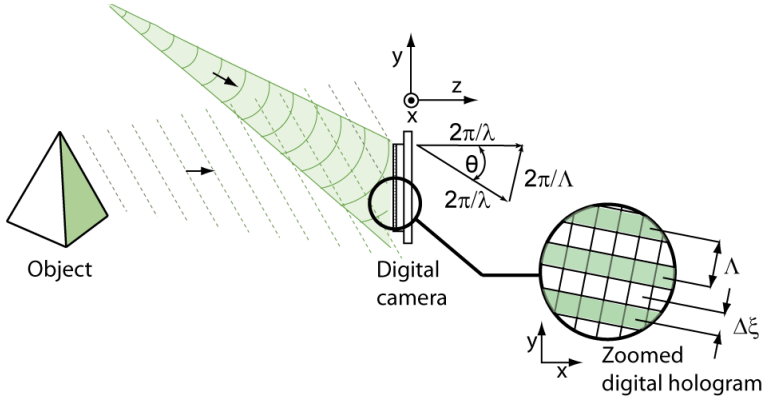

Figure 1.2: Recording of a digital hologram in off-axis arrangements. The pixelated digital sensor naturally samples the microinterference patterns. The boundary situation when the hologram fulfills the sampling criterion is outlined in the zoomed image.

The reconstruction in the conventional holography requires the illumination of the hologram by the reference wave. In digital holography this process is modeled numerically by a multiplication of the digital hologram representing by a transmittance h with the conjugated reference wave Ur^*. Further this wave field propagates from the hologram plane (with coordinates notation ξ,η) in a free space according to laws of diffraction and the resulting complex field is calculated in a certain reconstruction distance d – image plane (x,y).

In order to calculate complex amplitude U at image plane (x,y) we proceed from Kirchhoff integral:

$$U(x,y) = \frac{1}{j\lambda}\iint h(\xi,\eta)Ur^*(\xi,\eta)\frac{exp(jkr)}{r}d\xi d\eta, \tag{1.5}$$

where $r = \sqrt{d^2 + (\xi - x)^2 + (\eta - y)^2} = d\sqrt{1 + \frac{(\xi-x)^2+(\eta-y)^2}{d^2}}$. The Kirchhoff diffraction integral can be solved e.g. by Fresnel approximation (sometimes called Fresnel transformation). The Fresnel approximation omits third and higher terms of the Taylor series of function r in (1.5)(1.17). The Fresnel transformation reconstructs the complex amplitude in image by expression:

$$\begin{aligned} U(n\Delta x, m\Delta y) = {} & \frac{j}{d\lambda} exp\left(-\frac{j\pi}{\lambda d}[(n\Delta x)^2 + (m\Delta y)^2]\right) \\ & \times \sum_{n=1}^{N}\sum_{m=1}^{M} h(k\Delta\xi, l\Delta\eta)\, Ur^*(k\Delta\xi, l\Delta\eta) \times \\ & \times exp\left(-\frac{j\pi}{\lambda d}[(k\Delta\xi)^2 + (l\Delta\eta)^2]\right) \times \\ & \times exp\left(-j2\pi\left(\frac{kn}{N} + \frac{lm}{M}\right)\right) d\xi d\eta, \end{aligned} \tag{1.6}$$

Image plane resolution $\Delta x, \Delta y$ are given by the size of a frame $N\Delta\xi \times M\Delta\eta$, distance d and wavelength λ by equations:

$$\Delta x = \frac{\lambda d}{N\Delta\xi} \quad and \quad \Delta y = \frac{\lambda d}{M\Delta\eta}. \tag{1.7}$$

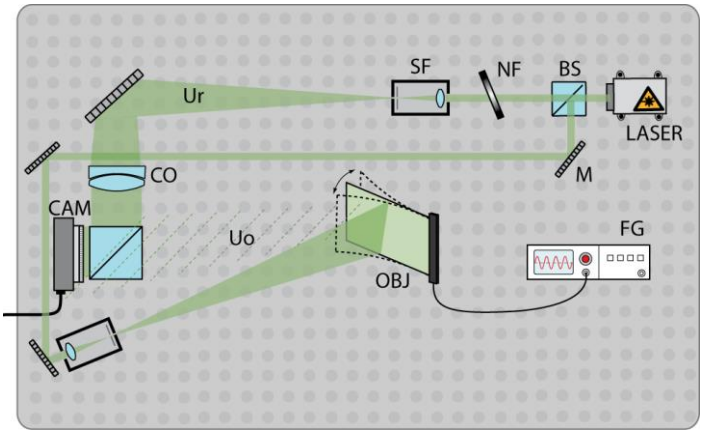

Figure 1.3: Principal scheme of a holographic interferometer employing components: BS - beam splitter, NF - neutral density filter, SF - spatial filter, CO - collimating objective, OBJ - object, FG - arbitrary waveform generator, CAM - digital camera, M - mirror, *Ur* denotes reference wave while *Uo* stands for object wave.

An example of off-axis digital holography is provided in Figure 1.3. The object - a steady beam cantilever - is $d = 0.6\,m$ apart from the sensor of AVT Stingray digital camera with parameters $N = M = 2048\,pix$ and $\Delta\xi = \Delta\eta = 3.45\,\mu m$. Light of wavelength $\lambda = 532nm$ was emitted by Nd:YAG laser. Digital hologram, as a result of interference between reference plane wave scattered from the object, is shown in Figure 1.4 (left). Field of intensity distribution calculated by Fresnel transform has a width of

$N\Delta x = \frac{\lambda d}{\Delta \xi} = 92.5\, mm.$ On closer examination of reconstruction equation (1.2) we can distinguish three different wave fields originating behind the hologram plane, see Figure 1.4 (right).

The real image corresponds to a wavefront converging to a sharp image, while the virtual image belongs to a divergent wavefront that seems to be not in focus. Another component, which can be seen in the intensity distribution image as a bright central square, is a d.c.-term. It is much brighter than the reconstructed real or virtual images. A mutual location of these components is given by the holographic setup, concretely, by angle of the reference and the object wave. If the angle is too small, the real image in Fourier domain is overlapped by the virtual image or by the d.c.-term. To suppress the overlapping we can change the holographic setup to have all components in frequency domain well separated. Further some numerical filters or phase shifting technique can be applied.

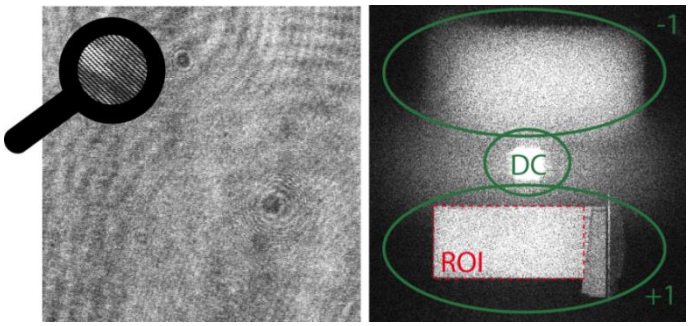

Figure 1.4: (left) Captured digital hologram with zoomed micro interference structure; (right) reconstructed intensity distribution by Fresnel transformation. Green ellipses denote different reconstructed diffraction orders and dashed red rectangle delineates the region of interest (ROI) – surface of the cantilever.

1.2 Time Average Digital Holography

The time average digital holography is used to measure the oscillation amplitude of diffusely reflecting object harmonically oscillating with an angular frequency ω. The displacement vector can be written as:

$$\boldsymbol{d}(R,t) = \boldsymbol{d}(R)\, sin\big(\omega t + \psi_0(R)\big). \qquad (1.8)$$

An equation for the object wave phase $\boldsymbol{\Omega}$ in relation on displacement vector $\boldsymbol{d}$ can be expressed as with definition of sensitivity vector $\boldsymbol{e}$[1]:

$$\Omega(R) = \boldsymbol{d}(R)\boldsymbol{e}(R). \qquad (1.9)$$

At any time t, the surface of the illuminated object diffuses an optical wave $\boldsymbol{U_o}$ with amplitude $U_0(R)$, written as:

[1] The simplest example is an out-of-plane vibrating surface in the z-direction with the sensitivity vector $e(p) = 4\pi/\lambda$

$$U_O(R,t) = U_0(R)exp(j\Omega(R)\,sin[\omega t + \psi_0(R)]), \tag{1.10}$$

The oscillating object is recorded holographically capturing a digital hologram according to equation $h \approx |U_o + U_r|^2$, see (1.1). Instantaneous hologram will be naturally time integrated over the exposure time T by the digital sensor:

$$h(\xi,\eta,0) = \int_0^T h(\xi,\eta,0,t)\,dt, \tag{1.11}$$

We can apply Fresnel transform in order to numerically reconstruct the complex field in the image plane. From (1.2) it is obvious, that the computed field is comprised of three different parts: real image, virtual image and dc term. The complex field of the real image carrying information of the object wave is proportional to:

$$U_{real}(R,t) \approx \int_0^T U_0(R)exp(j\Omega(R)\,sin[\omega t + \psi_0(R)])\,dt. \tag{1.12}$$

By proper combination of the power series components and using the Euler formula we obtain the formula:

$$\sum_{n=0}^{\infty} J_n(A)\,exp(jnB) = exp(jA\,sin(B)), \tag{1.13}$$

where J_n is the *n-th* kind zero-order Bessel function. Applying (1.13) on (1.12), the complex field becomes:

$$\begin{aligned} U_{real}(R,t) &\approx \int_0^T \sum_{n=0}^{\infty} U_0(R)J_n\big(\Omega(R)\big)\,exp(jn[\omega t + \psi_0(R)])\,dt = \\ &= \sum_{n=0}^{\infty} U_0(R)J_n\big(\Omega(R)\big) \int_0^T exp(jn[\omega t + \psi_0(R)])\,dt. \end{aligned} \tag{1.14}$$

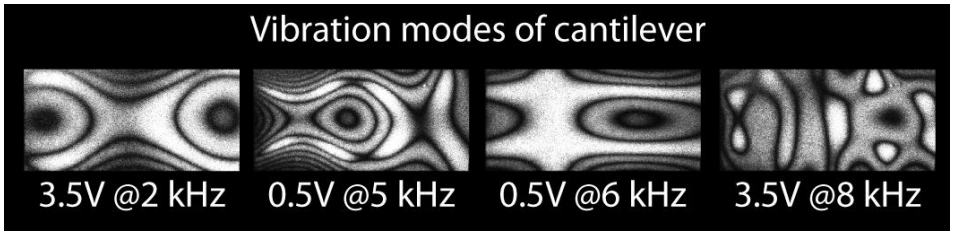

Figure 1.5: Intensity distributions reflecting vibration modes of the cantilever visualized by time average digital holography. The modes of the cantilever's vibrations strongly depend on driving frequency.

In time average holography the exposure time is much longer when compared to the period of the vibration of the object[2] $T \gg 2\pi/\omega$. The averaging process can be mathematically expressed by limit as time approaches infinity and therefore:

[2] A typical exposure time in time average digital holography is set to be $T \approx 1\,s$ while the period of the vibrations (100 Hz) starts at $\frac{2\pi}{\omega} \approx 0.01\,s$.

$$U_{Real}(R) = \lim_{T\to\infty} \sum_{n=0}^{\infty} U_0(R) J_n\big(\Omega(R)\big) \int_0^T exp(jn[\omega t + \psi_0(R)])\, dt = U_0(R) J_0(\Omega(R)). \tag{1.15}$$

Due to the integral in (1.15), the term vanishes for all n except *n=0.* The reconstructed intensity in the image plane is expressed as:

$$I(R) = |U(R)|^2 = I_0(R) {J_0}^2\big(\Omega(R)\big), \tag{1.16}$$

where I_0 denotes intensity distribution of the object without presence of oscillation and can be considered unity.

Some results obtained by time average digital holography are in Figure 1.5 and Figure 1.6. The beam cantilever from the example outlined in Figure 1.3 was driven by harmonic voltage signal with different magnitudes and frequencies. One should note that the holographical arrangement remains the same and only the ROI is displayed.

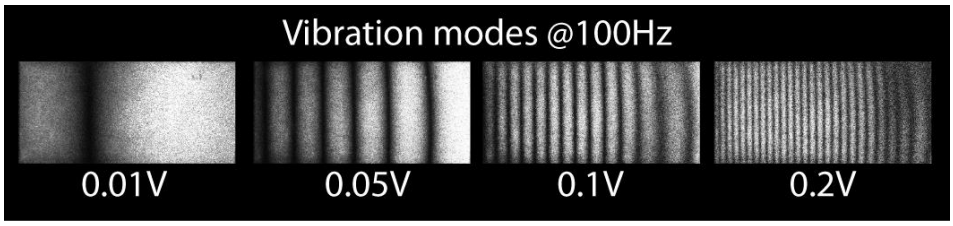

Figure 1.6: Intensity maps of oscillating cantilever at frequency 100 Hz obtained by time average digital holography. Not surprisingly holds that the greater supplying voltage generates greater amplitudes of vibrations.

The range of measureable amplitudes by the method is limited from the both sides. For very small amplitudes $\Omega \to 0$, the sensitivity of time average method is approaching zero:

$$\lim_{\Omega\to 0} \frac{dJ_0}{d\Omega} = 0. \tag{1.17}$$

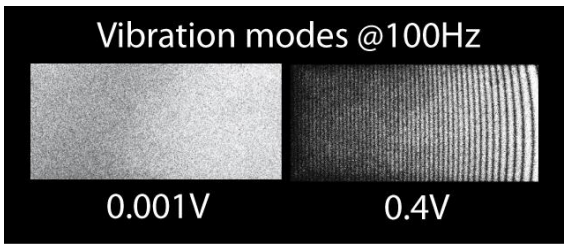

Figure 1.7: Limits of time average digital holography for small amplitudes (left) and great amplitudes (right) of vibrations.

In practice, for very small amplitudes bellow approximately 30 nm we obtain more or less uniformly distributed intensity map as can be seen in Figure 1.7 (left).

On the other hand measurement of large amplitudes is also limited. It is obvious that the method works unless the dark fringes in the magnitude field are resolvable, see Figure 1.7 (right). Such intensity map corresponds to amplitude distribution with maximal value of approximately $5\ \mu m$.

2 Extension of measurement capabilities of time average digital holography

2.1 Employment of acusto-optical modulators in holographic arrangements

Acusto-optical modulator uses the interaction of a column of traveling acoustic waves with an incident coherent optical beam to modulate the properties of the transmitted optical wavefront. The modulator consists of a transparent medium into which acoustic waves can be launched by a piezoelectric transducer. The transducer is driven by radio frequency voltage source and launches a compressional into the acoustic medium. The acoustic wave propagates in the medium through small local displacements of molecules leading to strain in the medium. Associated with these strains are small changes of the local refractive index, a phenomenon known as the acousto-optic or the photo-elastic effect.

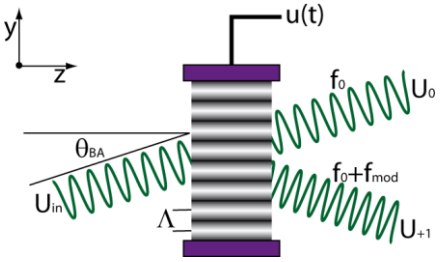

Figure 2.1: Acusto-optical modulator in Bragg regime – Bragg cell.

In Bragg regime, which is the subject of our concern, the RF frequencies are in the hundreds of MHz to the GHz range. The optical frequency of the 1st diffraction order can be determined from the Doppler-shift relation

$$f_1 \approx f_0 + f_{mod}. \qquad (2.1)$$

Thus the optical frequency of the 1st diffraction order is translated by the driven frequency f_{mod}.

Until now the voltage driving the acousto-optic cell has been assumed to be a perfect continuous wave (CW) signal. However, phase ϕ or amplitude A modulation of driven voltage has a great importance for time average digital holography improvement as will be shown. The complex amplitude transmitted into the first diffraction in order of phase modulated driven signal order is given by

$$U_{+1}(y,t) = \frac{\pi dC}{\lambda} U_{in} A(t-\tau) exp\left(-j\phi(t-\tau)\right) \times \\ \times exp\left(j\frac{2\pi y}{\Lambda}\right) exp(j2\pi f_{mod}(t-t_0)), \tag{2.2}$$

where U_{in} is the complex amplitude of the incident monochromatic optical wave, C is a proportionality constant and $\tau = t_0 - y/v$.

Introducing Bragg cells into the both arms of holographical arrangements, as illustrated in Figure 2.2, we can take advantage of the frequency and phase modulation generated by the Bragg cells in order to extend measurement capabilities of the time average digital holography. The object U_o and the reference U_r wave are further modulated by the acousto-optic cells placed in the object and the reference arm U_{BCo}, U_{BCr} in compliance with equation (2.2). The interference formula (1.1) for recording of digital hologram becomes more general:

$$h \approx |U_o U_{BCo} + U_r U_{BCr}|^2 = \\ = |U_o U_{BCo}|^2 + |U_r U_{BCr}|^2 + U_o U_{BCo} U_r{}^* U_{BCr}{}^* + U_o{}^* U_{BCo}{}^* U_r U_{BCr}. \tag{2.3}$$

and parameters of the modulation (A, ϕ, f_{mod}) influence properties of the reconstructed wave field.

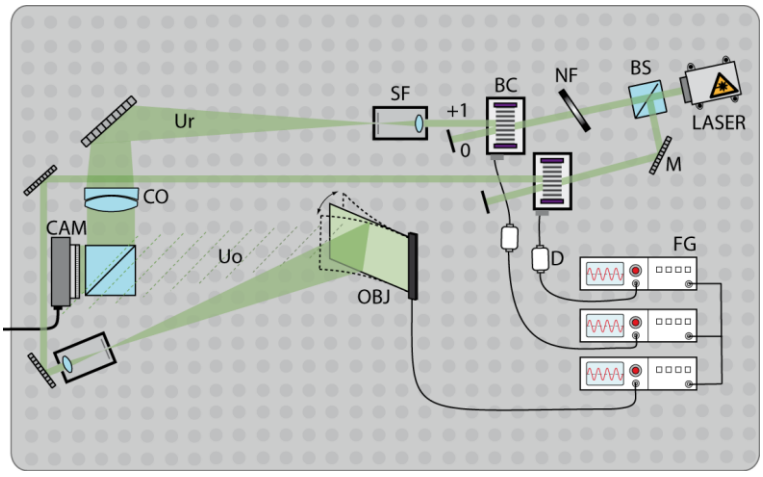

Figure 2.2: Principal scheme of an experimental arrangement for time average digital holography measurement with the employment of Bragg-cells (BC).

2.2 Improvement of lateral resolution and SNR by heterodyne interferometry

The reconstructed optical field propagating behind hologram consists of three different diffraction orders. However, only the real image represented by term $I_r U_0$ carries the required information. The remaining terms act only as a disturbing signal. Angle ϑ between the object wave and the plane reference wave $U_r = exp(-jkx\,sin(\vartheta))$ defines the mutual location of the real image, the virtual image and the d.c. term in the image plane. The limiting value $\vartheta = 0$ leads to in-line holography where all the terms overlap each other.

For further analysis it is illustrative to examine the reconstructed field behind the hologram in spectral domain. Considering $\mathcal{U}_r, \mathcal{U}_o$, and $\mathcal{H}$ to be Fourier images of U_r, U_o, and h can be rewritten as:

$$\mathcal{H} \approx \delta \star \delta + \mathcal{U}_o \star \mathcal{U}_o + \mathcal{U}_o * \delta + \delta * \mathcal{U}_o{}^* = \delta + \mathcal{U}_o \star \mathcal{U}_o + \mathcal{U}_o + \mathcal{U}_o{}^*. \qquad (2.4)$$

where symbols $*,\star$ denote convolution and correlation, respectively. Graphical interpretation of (2.4) is shown in Figure 2.3 (left).

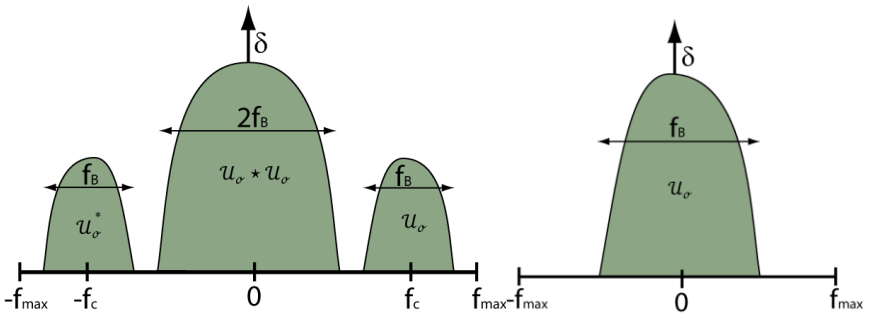

Figure 2.3: 1D outline of spectral domain of an off-axis (left) and in-line (right) digital hologram after suppression of the undesired terms.

The central part of the hologram spectrum is known as the autocorrelation term. Separation of the terms in spectral domain is driven by the carrier frequency f_c that is directly affected by angle of the reference wave ϑ. From one side, the maximal value of ϑ is limited by Nyquist. On contrary, the individual terms cannot overlap each other and therefore the carrier frequency must be sufficiently great. Even though the carrier frequency is set to be optimal, the width of spectrum belonging to useful information $\mathcal{U}_o$ is restricted to approximately one fourth of the spectrum width $\langle -f_{max}, f_{max} \rangle$.

To improve the reconstruction quality and lateral resolution, d.c. term and twin image terms have to be canceled. Once the undesired terms in the spectrum are suppressed, we can set $f_c = 0$ in the manner of in-line digital holography and bring the object closer to the detector. Thus the bandwidth of the object widens, which results in improvement of the lateral resolution in image plane according to formula (1.7). Obviously, the noise in the hologram or image plane generated by contributions from the d.c. term and the virtual image is also suppressed, which enhances signal-to-noise ratio (SNR).

The suppression of the d.c. term and the virtual image can be achieved by so called phase-shifting technique, where the complex field in hologram plane is calculated from at least three digital holograms with a mutual phase shift in the reference wave. The calculated complex field represents only contribution from the real image and thus is free of the virtual image and the d.c. term.

Let us again consider the diffracted field in the hologram plane (1.1) in general form

$$h \approx a + b\,cos(\varphi_o), \qquad (2.5)$$

where additional term $a = |U_r|^2 + |U_o|^2$ is average intensity of the hologram and multiplicative term $b = 2|U_r||U_o|$ expresses intensity modulation.
The aim is to calculate complex field of the object wave $U_0 = |U_o|\exp(-j\varphi_o)$, that is obviously proportional to the real image. The magnitude $|U_o| = \sqrt{I_o}$ can be easily measured; however, $|U_o|$ acts only as a normalization factor and therefore can be set unity. The unknown phase field φ_o must be calculated accurately. Formula (2.5) contains three unknowns variables and therefore not a single, but at least three digital holograms with well-defined phase shifts $\Delta\varphi$ introduced into the reference beam or the object beam must be captured. This leads to set of N equations:

$$h_i \approx a + b\,cos(\varphi_o + \Delta\varphi_i), \qquad (2.6)$$

where i denotes an integer $i = 1,2,3,\dots N$. The unknown phase φ_o can be calculated as a solution of the set of equations.
The holographical arrangement is illustrated in Figure 2.2. The Brag cell in reference arm and object arm is driven by sinusoidal voltage of frequency f_{R-mod} , f_{O-mod}, respectively. Reference and object beams are temporally modulated by frequency $\omega_r = 2\pi(f_0 + f_{R-mod})$, respectively, $\omega_O = 2\pi(f_0 + f_{O-mod})$, where f_0 is working RF frequency of Bragg cells. If $\omega_R \neq \omega_O$, the frequency shift in one of the interfering light waves can be envisaged as a continuous shift of the mutual phase between the light waves:

$$h \approx a + b\,cos(\varphi_o + (\omega_O - \omega_R)t). \qquad (2.7)$$

The intensity at each point of the digital hologram varies as a sinusoidal function with the beat frequency $\omega_B = 2(\omega_O - \omega_R) = 2\Delta\omega$. The interference of two optical waves of different frequencies is a basis of so called heterodyne technique. We need to sample the temporal varying digital hologram with required phase shift $\Delta\varphi_i$ in order to substitute these values in (2.6). The inherent temporal sampler in digital holography is a digital sensor via its frame rate FPS. The relative phase shift $\Delta\varphi$ between two consecutive digital holograms is:

$$\Delta\varphi(\Delta\omega) = \varphi(t) - \varphi\left(t + \frac{1}{FPS}\right) = (\omega_O - \omega_R)\frac{1}{FPS} = \frac{\Delta\omega}{FPS}. \qquad (2.8)$$

Formula shows that we can generate arbitrary phase shift $\Delta\varphi$ between frames of the digital sensor by driving the frequency of Brag cells. This can be favorable used in solution of the set of equations defined in (2.6).
The most straightforward phase-shifting approach is a four step algorithm. The four step algorithm requires that four separate digital holograms are recorded. An optical phase shift $\Delta\varphi = \pi/2$ is introduced between each of the sequentially recorded holograms in the manner of (2.8).

Finally, the transmittance (digital hologram) h in the reconstruction formula can be replaced by the computed complex transmittance function of object wave in the hologram plane U_0.

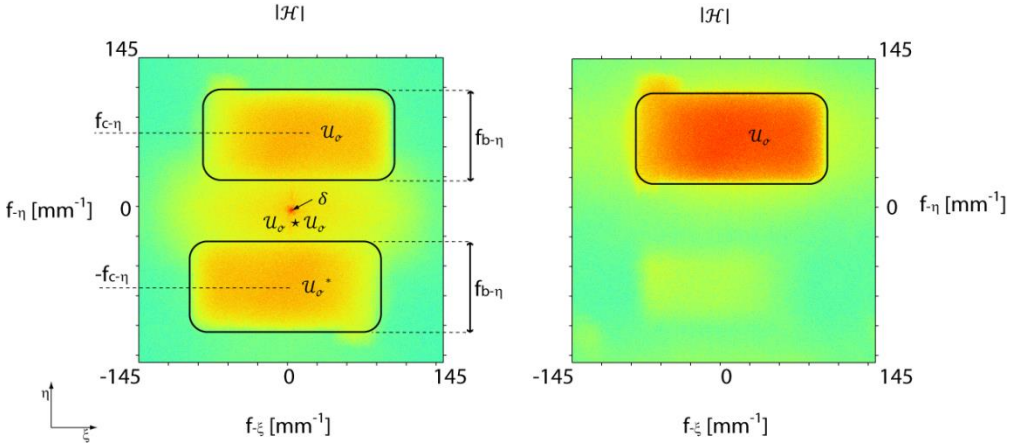

Figure 2.4: Spectral domain of off-axis digital hologram without (left) and with (right) phase shifting technique. False colors represent magnitude of the spectrum in a logarithmic scale.

An example of magnitude spectra computed in case of single capture digital holography and phase-shiting digital holography is presented in Figure 2.4. The spectrum shown on the right hand side bears particularly information about the object wave while the twin image and the autocorrelation term are strongly suppressed.

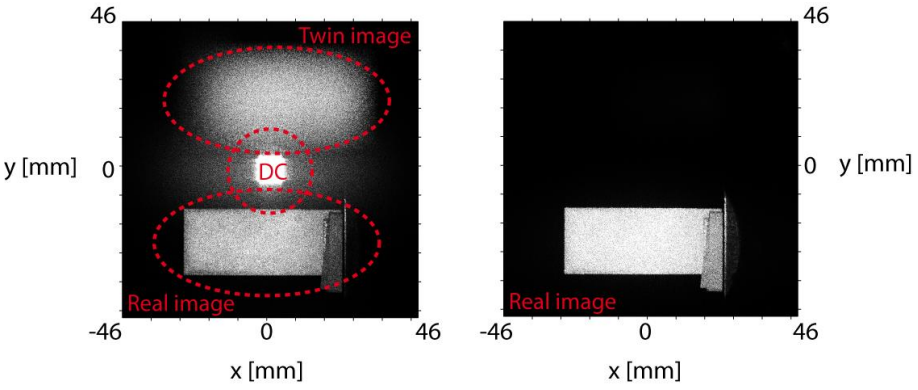

Figure 2.5: Reconstructed intensity field in image plane in case of off-axis arrangements without (left) and with (right) phase shifting technique.

It is clearly seen the improvement of SNR in case of phase-shifting technique. Reconstructed intensity distribution in image, which is the main subject of concern, is then shown in Figure 2.5 right. The power of the real image signal[3] η with $N_{\mathcal{U}_o}$ elements defined as $\eta = \sum_{f_b} |\mathcal{U}_o(f_b)|^2 / N_{\mathcal{U}_o}$ is about 30% better in case when phase-shifting technique is employed, which helps to improve the recovered information and makes

[3]The power spectrum η can be regarded as a diffraction efficiency of a diffraction grating at certain spatial frequency.

the time average holography more sensitive. In next step one can place the object closer to digital sensor in order to improve the lateral resolution, see (1.7).

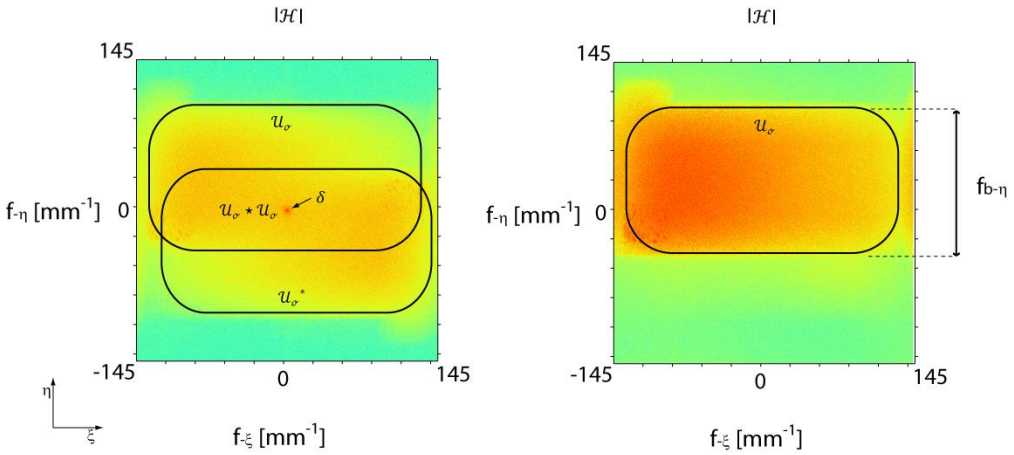

Figure 2.6: Spectral domain of in-line digital hologram without (left) and with (right) phase shifting technique. False colors represent magnitude of the spectrum in a logarithmic scale.

Results of the same object in this case placed closer to digital camera are introduced in Figure 2.6 and Figure 2.7.

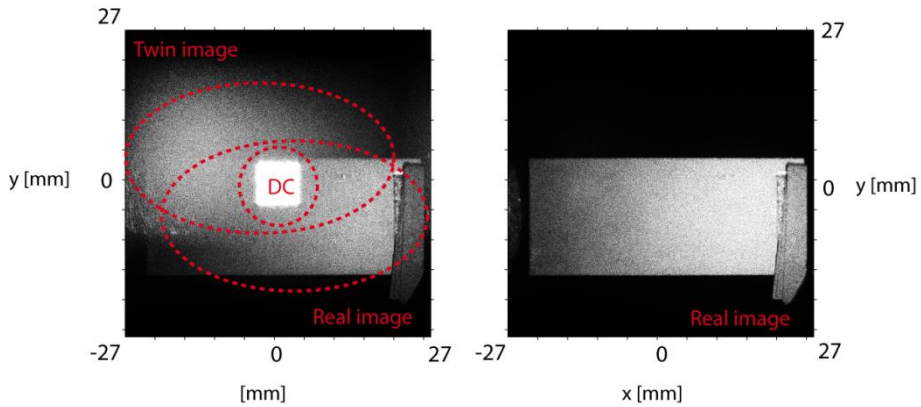

Figure 2.7: Reconstructed intensity field in image plane in case of in-line arrangements without (left) and with (right) phase shifting technique.

2.3 Extension of dynamic range by means of frequency modulation

The dynamic range of measurable amplitudes by time average digital holography was estimated to be in the range starting from approximately 100 nm to few microns, see chapter 1.2. For smaller amplitudes the first limiting factor is the amplitude retrieval by interpolation of a sparse array of known values. This limit is just a subject of calculation, however, when approaching zero (order of nm), the sensitivity of time average method decreases and falls to zero, see (1.17). The upper bound is limited to situation where fringes in the intensity field can be counted. Otherwise, it becomes difficult to count many narrow fringes, and even impossible when they are smaller than

the optical resolution. Frequency modulation introduced in one of the arm can address the above mentioned problem and shift the limits of time average holography.
Let´s start with arrangement shown in Figure 2.2. Oscillating object modulates phase of the object wave in the same manner as described in (1.10). Applying a sinusoidal signal with frequency $f_0 + f_{R-mod}$ to the Bragg cell placed in reference arm results in frequency modulation of the reference wave: $U_{BCr} = exp(j2\pi(f_0 + f_{R-mod})t) = exp(j(\omega_0 + \omega_{R-mod})t)$. As will be demonstrated, it is advantageous when the reference wave is modulated by an integer multiple $\omega_{R-mod} = m\omega$ of the object vibration frequency ω. Further steps are identical with those in chapter 1.2 with exception of the presence of the frequency modulation. The reconstructed magnitude of the real image:

$$|U(R)| \approx \left|J_m\big(\Omega(R)\big)\right|. \qquad (2.9)$$

is modulated by m-th order Bessel function. In conclusion, controlling the frequency shift of reference (or object) wave about integer multiple of the object vibration frequency allows for control of order of Bessel function modulating the resulting intensity field. Results of experiment carried out in order to prove formula (2.9) are presented in Figure 2.8.

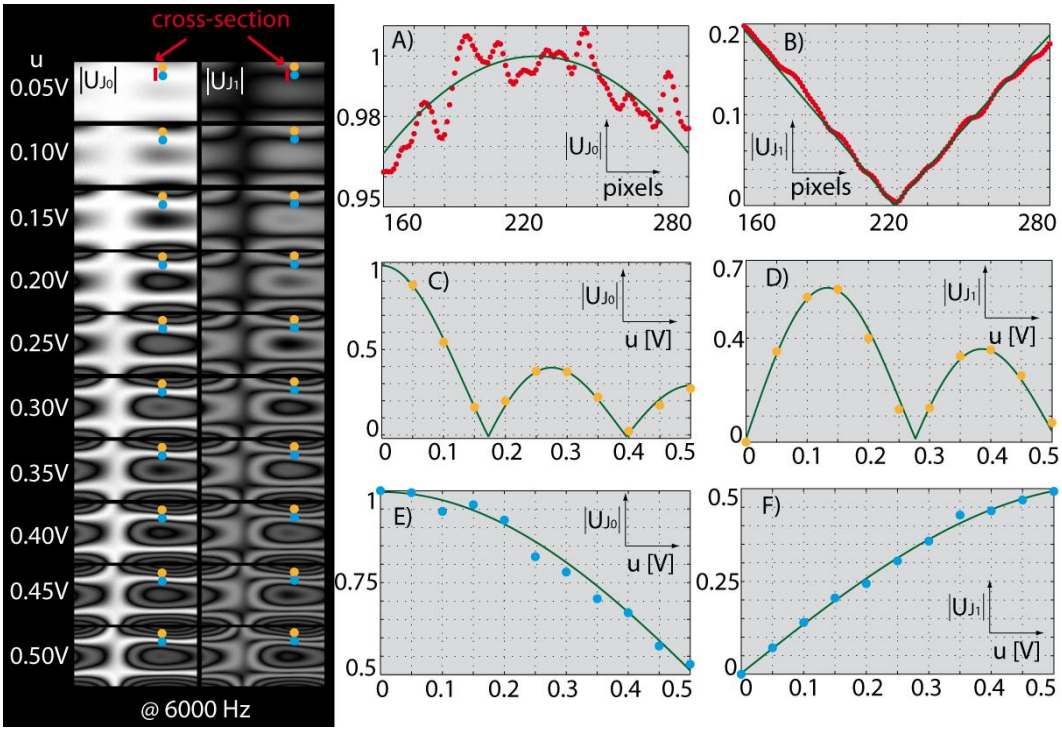

Figure 2.8: (black frame) Impact of frequency modulation on magnitude maps when increasing the supply voltage; (A, B) Measured values (red points) and theoretical values (green line) along cross-section denoted by the red line in magnitude map for 0.05V. Left plot (A) stands for non-modulated holography, where the sensitivity and SNR is obviously lower when compared to modulated technique introduced in the right plot (B); (C, D, E, F) As the supply voltage increases, the magnitude in each pixel varies. Magnitude variations at two pixels denoted by orange and blue circle were investigated in

detail and compared to theoretical curves (green line). This was done for non-modulated (C, D) as well as modulated (D, F) technique.

Time-average holography with frequency modulation can be used to increase the sensitivity for vibrations with small as well as with large amplitudes. In time average holography with no modulation, the magnitude of reconstructed field $|U| \approx |J_0(0)|$ is unity and has slope zero (1.17). On the other hand when *m=1*, $|U| \approx |J_1(0)|$ has a positive slope in the dark field:

$$\lim_{\Omega \to 0} \frac{dJ_1}{d\Omega} = 0.5 \qquad (2.10)$$

yielding visible intensity variations even for small amplitudes.

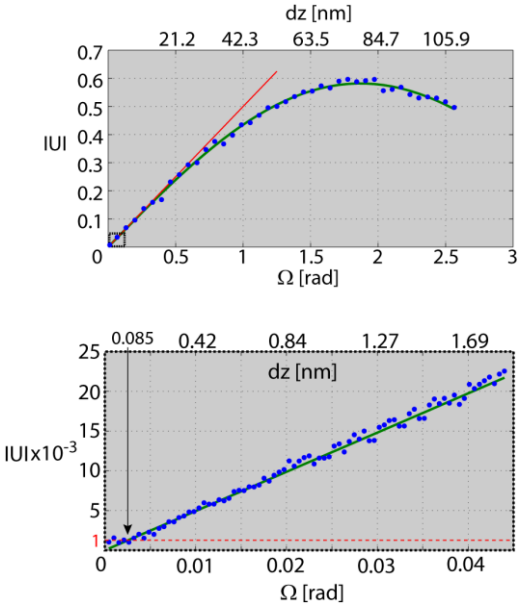

Figure 2.9: Values of magnitude at blue point with increasing supply voltage. The independent axis is calibrated to argument of the Bessel function. The red line marks out the noise level and the lowest measurable amplitude.

In order to determine the smallest measurable amplitude by the frequency modulated holography for our experimental arrangement, measurements with fine steps 0.05mV of supply voltage for extremely small values (0 – 4 mV) was conducted. The aim was to find thresh of the supply voltage (indeed vibration amplitude) where the noise represses the measured signal. The graphically interpreted results of blue point are plotted in Figure 2.9. The upper graph represents coarse measurement executed in great supply voltage range. The "coarse" measurement serves for calibration of independent (x) axis scale in order to obtain dependence on argument of Bessel function $\Omega = \frac{4\pi}{\lambda} d_z$ defined in (1.9) instead of supply voltage. For small amplitudes where $\Omega < 0.5$ the Bessel function can be approximated by linear function $J_1(\Omega) \approx \frac{1}{2}\Omega$, see red line in Figure 2.9. The graph lower shows results of the "fine" measurement in the very small interval of supply voltages (small amplitudes). When approaching zero, the measured values (blue

circles) follow the theoretical value up to $|U_{J1}|$~0.001. Considering the linear approximation:

$$d_z = 2\frac{\lambda}{4\pi}|U_{J1}|, \qquad (2.11)$$

the smallest measureable amplitude reaches d_z~0.085 nm or in terms of wavelength $d_z \sim \frac{\lambda}{6000}$.

The same measurement procedure was repeated for pixel placed in different position of the surface denoted by the violet circle. As obvious from, the smallest measureable amplitude is five times greater if compared with the blue point: d_z~0.42 nm. At first sight it seems to be in contrary with the "blue point" measurement, however, the performed analysis has clarified the apparent discrepancy.

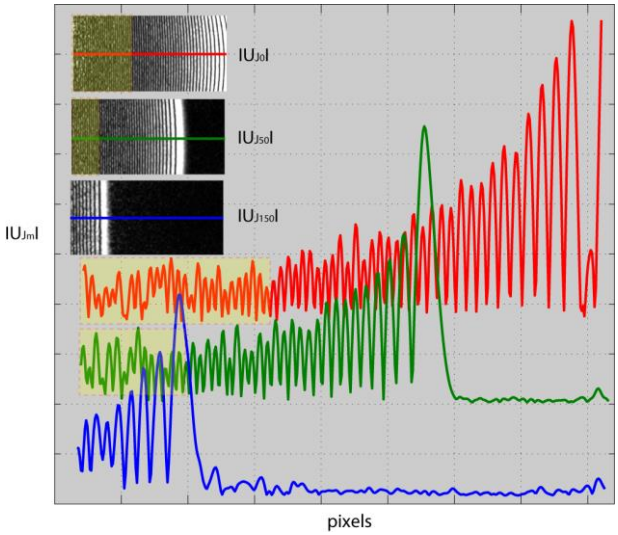

Figure 2.10: Frequency modulation used for large amplitudes of vibrations. Red line represents magnitude cross-section of non-modulated technique, wile green and blue lines represent modulation of order m=50 respectively m=150.

In the case of large vibration amplitudes we take advantage of the fact that the locations of the zeros of the Bessel functions are spread apart for increasing order m. As a consequence the number of fringes for the same amplitudes decreases with increasing m and therefore too high fringe densities can be effectively avoided. An example is introduced in Figure 2.10.

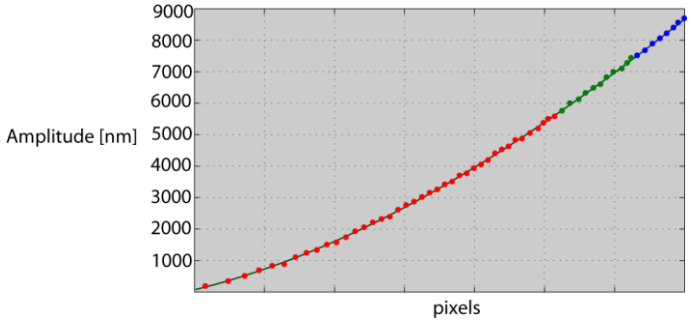

Figure 2.11: Amplitude of vibrations along the cantilever cross-section.

The yellow rectangle covers the region, where the density of fringes is unresolvable due to speckles. Shifting the frequency of the reference wave about a fifty times multiple of the object oscillations frequency $f_r = f_0 + mf = 40MHz + 50 * 100Hz$ results in magnitude distribution $|U_{J50}|$. The yellow rectangle has shifted closer to the edge of the cantilever as the measurement range has. One dimensional cross-section is denoted by the green curve in Figure 2.10. Although the measurement range has been extended using $|U_{J50}|$, still, the fringe pattern in very close region to the edge is not resolvable. Applying m=150 one can shift the measurement range even closer to the edge of the cantilever and by proper combination of zeroes extracted from magnitudes $|U_{J0}|, |U_{J50}|$ and $|U_{J150}|$ the amplitude distribution can be evaluated over the whole surface, see Figure 2.11.

2.4 Evaluation of vibration amplitude independently in every pixel using phase modulation

So far we have only assumed a harmonic signal which drives the Bragg cells. The driving harmonic signal lead to frequency modulation, when the optical frequency of the 1st diffraction order is translated by the working frequency f_0[4]. However, phase-modulated CW signal can also be used, as it was already mentioned. In this chapter, it will be shown how the phase modulation of the reference arm influences behavior of the time-average holography and how it can be exploited for quantitative analysis of vibrations amplitudes.

The real image of diffracted field in image plane, when the phase modulation is applied:

$$|U_{real}| \approx |J_0(\Omega - \phi_{BC})|. \qquad (2.12)$$

is computed by e.g. Fresnel transform.

Now the loci of bright zero fringes are controllable by the user, since they appear where $\Omega = \phi_{BC}$. In order to verify the formula (2.12) a fine tuning of the modulation depth ϕ_{BC} was experimentally performed, see Figure 2.12. For more detailed analysis four representative pixels denoted by letters A, B, C, D in Figure 2.12 (right) were picked. In these points magnitude versus modulation depth with the fine steps was evaluated. Although some noise is presented, the magnitude follows the formula $|J_0(\Omega - \phi_{BC})|$ with the increasing modulation depth within the half interval $\langle 0, \pi \rangle$ radians that creates period of the signal. These results can be consequently used for independent evaluation of vibrations amplitudes in every single pixel.

In chapter 2.2 it was introduced, how to recover argument[5] of cosine function encoded in set of phase-shifted intensity field (2.6). Easy use of phase-shifting interferometry is derived from the harmonic cosine nature of interference fringes. In time average holography the intensity is modulated by Bessel functions. Unfortunately, the Bessel

[4] Let us remind working frequency $f_0 = 40\ MHz$ for the Bragg cells used within scope of this work.

[5] In this case argument of cosine function physically represents phase between the reference and the object beam.

function of a sum cannot be expressed as a sum of terms and therefore the straightforward phase recovery in the very same way as for cosine fringes is not possible. However, a possible solution is to make use of a nearly periodic nature of the Bessel functions and regard the modulation to be cosine.

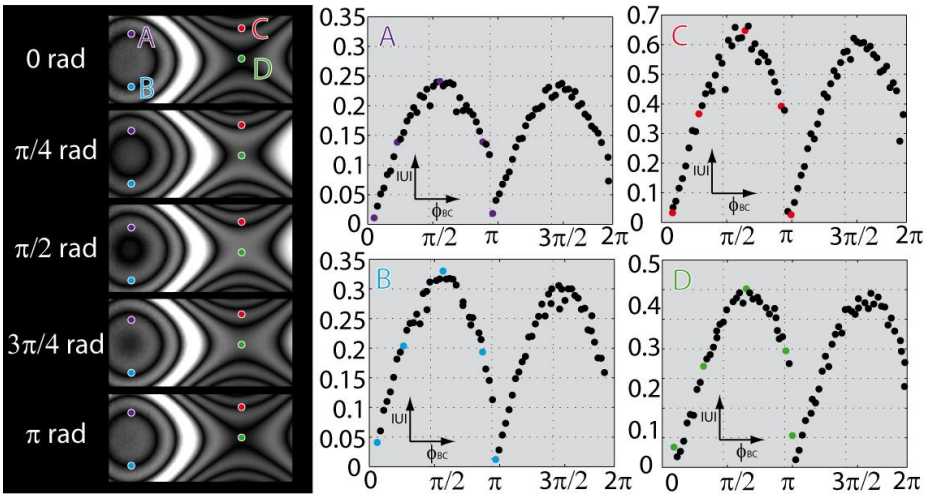

Figure 2.12: (black frame) Magnitude maps of an oscillating cantilever with different phase offsets; (right) Magnitude values at four points (A, B, C, D) are plotted as a function of the phase offset (colored point correspond to magnitude maps in black frame).

Replacing the real argument Ω with approximate argument Ω^* the phase-shifting approach can be applied. We first have to capture and reconstruct set of time average digital holograms with different phase offsets ϕ_{BC}:

$$|U_i| = a + b|J_0(\Omega - \phi_{BCi})| \sim a + b|cos(\Omega^* - \phi_{BCi})|, \qquad (2.13)$$

where additional term a is average value of the object field and multiplicative term b is the object field in the absence of oscillations. Assuming four-step algorithm, an optical phase shift about one fourth of the period, $\phi_{BCi} = \pi/4$, is introduced between each of the reconstructed amplitudes of object field. These four equations in three unknowns a, b, Ω can be solved at each point of the reconstructed field and the approximate argument Ω^* can be computed by formula:

$$\Omega^* = atan\left(\frac{|U_4| - |U_2|}{|U_1| - |U_3|}\right). \qquad (2.14)$$

Since the arctangent function is bounded, the resulting phase (or argument of the Bessel function) Ω^* is wrapped within interval $\langle -\pi, \pi \rangle$[6]. Such a wrapped field must be unwrapped in order to obtain phase distribution free of the 2π jumps.

[6] The scale of arctangent function is $\langle -\pi/2, \pi/2 \rangle$ but it is good practice to consider the signs of the numerator and the denominator separately e.g. by ATAN2 function in MatLab.

The approximate unwrapped phase Ω^* differs from the real argument of Bessel function Ω due to not perfectly periodic nature of Bessel function. The difference $\Delta = \Omega - \Omega^*$ is calculated as an angle between $|cos\, x|$ and $|J_0(x)|$. Once the angle difference is known, the approximate phase is corrected in order to get real argument of the Bessel function $\Omega = \Omega^* + \Delta$. The amplitude distribution measured by this method is introduced in Figure 2.12 together with the wrapped phase Ω^* and corrected unwrapped phase Ω. It is very important to note, that the phase shifting technique unlike other vibrations amplitude retrieval approaches is sensitive to sign of mechanical phase of vibrations.

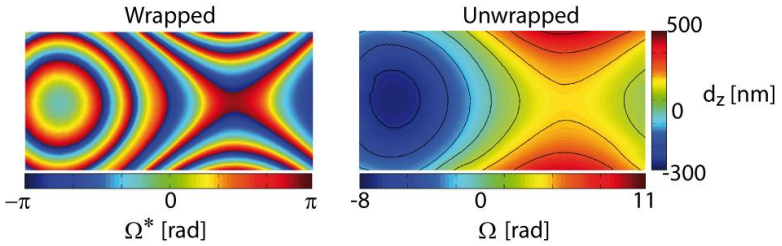

Figure 2.13: Wrapped phase with value within interval $\langle -\pi, \pi \rangle$ (left) and corrected unwrapped phase (right) without the phase jumps. Since phase is linearly proportional to amplitude of vibrations, vertical colorbar stands for values of amplitudes of vibrations.

A sequence of measurements at different times was done in order to asses a repeatability of the method. The total number of conducted measurement was 15. The set of measured amplitude distributions was analyzed by means of basic statistical tools. The averaged amplitude distributions (Figure 2.14) $\overline{d_z(R)} = \frac{1}{N}\sum_{n=1}^{N} d_{z\,n}(R)$ as well as standard deviation along cross-section denoted by green line $\sigma(R) = \sqrt{\frac{1}{N}\sum_{n=1}^{N}\left(d_{z\,n}(R) - \overline{d_z(R)}\right)^2}$ are shown in Figure 2.15.

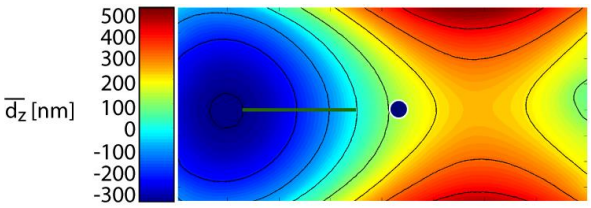

Figure 2.14: Amplitude distribution averaged from 15 measurements. Green cross-section and blue point are used for further analysis.

The standard deviation defines "type A" uncertainty representing primarily random noise presented in the measurement procedure. Noise usually consists of an additional and multiplicative part. In the same manner one can define the standard deviation as $\sigma(R) = \mathrm{A} + \mathrm{B}\,\overline{d_z(R)}$[7]. After fitting the measured data, standard deviation is determined as:

$$\sigma(R) = 0.05 + 0.01\,\overline{d_z(R)}\ [nm], \qquad (2.15)$$

[7] The standard deviation σ depends furthermore on values of magnitude fields. Therefore the formula is also influenced by Bessel function, however, this influence was omitted in order to stay clear

or in terms of percentage of the measured amplitude $\frac{100\sigma}{\overline{d_z}} = \frac{5}{\overline{d_z}} + 1\,[\%]$. Considering value $\overline{d_z} = 300\,nm$, the standard deviations becomes $\sigma = 3.05\,nm \sim 1.17\,\%$. Standard deviation σ accounts for 68.27 percent of the Gaussian function; while three standard deviations account for 99.73 percent. In other words, results of almost all measurements fall into interval of 3σ, what means $3\sigma = 9.2\,nm \sim 3.5\,\%$ for the measurement around $\overline{d_z} = 300\,nm$. One should note, that this kind of analysis does not include evaluations of all contributions to the dispersion of values that might reasonably be attributed to the measurand.

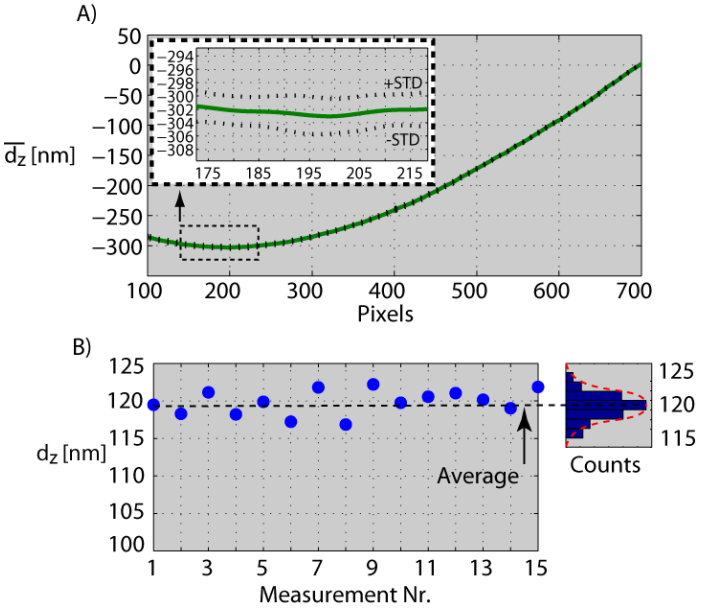

Figure 2.15: (A) Averaged values of vibrations amplitudes along the green cross-section (green curve) and interval determined by standard deviation (black dotted curves); (B) fifteen measurements of vibrations amplitudes at the blue point that are spread around the average according to laws of normal distribution as can be observed in the histogram plot

2.5 Discussions and conclusions

Three techniques for improving of time average digital holography have been introduced in chapter three. Namely it is:

- Heterodyne detection
- Frequency modulation
- Phase modulation

Although all the methods were introducing individually for clarity reasons, they share identical hardware requirements and can be arbitrarily combined. Remind the experimental arrangements outlined in Figure 2.2. The frequency and phase modulated driven voltage is transformed via the Bragg cell into the 1st order wavefront described by:

$$U_{BCr} = exp(-j\phi)exp(j2\pi f_{R-mod})) \qquad (2.16)$$

in case of reference wave and

$$U_{BCo} = exp(j2\pi f_{R-mod})) \tag{2.17}$$

for the object wave. The reference beam is phase modulated at frequency ω of the vibrating object with a modulation depth ϕ_{BC}: $\phi = \phi_{BC}\sin(\omega t)$ while the frequency is shifted about integer m of frequency of the object f and one fourth of digital camera frame rate FPS in order to employ heterodyne technique with $\pi/2$ phase shifts between holograms[8]: $f_{R-mod} = f_0 + mf + FPS/4$. This finally leads to formula

$$|U_{real}| \approx |U_0||J_n(\Omega - \phi_{BC})|. \tag{2.18}$$

Formula (2.18) includes all advantages described separately in previous subsections. Combination of the three approaches was used for measurement of cantilever vibrating at 1000Hz. The supplying voltage of the cantilever started at $200\,\mu V$ and finished at $200\,V$. Logarithmic increment steps of supplying voltage were chosen instead of linear due to a huge amount of measurements. Results of the measurement are introduced in Figure 2.16. Measured values (blue points) follow the theoretical values (red dashed line) down to approximately $0.1\,nm$. This noise level has been derived previously. As obvious from scale of the plot in Figure 2.16, the dynamic range of the measurement is 100000.

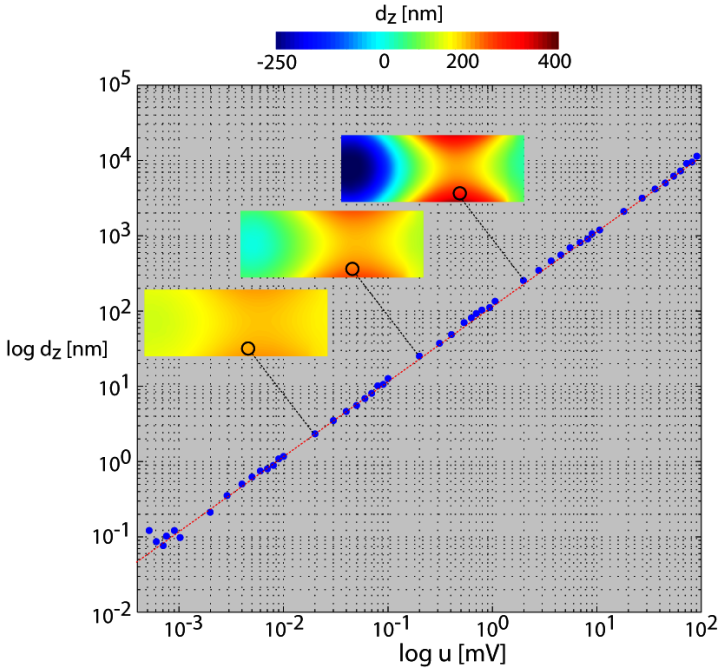

Figure 2.16: Measured amplitudes of vibrations of the beam cantilever at different supply voltages. Blue points determine value of amplitude of vibrations in the marked position. Some amplitude maps of the whole surface are also introduced and linked to corresponding measurement.

[8] In general, one can use FPS/M, where M is an integer in order to generate phase shifts appropriate for the used phase-shifting algorithm.

It is worthwhile to mention some sources of distortions degrading the magnitude distribution. A typical intensity distribution is disturbed by the low frequency background intensity caused by a varying illumination, e.g. a Gaussian profile of the expanded laser beam, or a changing object reflectivity. Further it is the fringe visibility influenced mainly by the ratio between the reference and object wave amplitudes. The magnitude variation caused by the speckles, which act as signal dependent coherent noise. The electronic noise originates in photodetectors or waveform generators supplying the Bragg cells. In practical applications of holographic interferometry electronic noise plays a minor role as compared to the speckle noise. So normally no special care is taken regarding electronic noise. Finally diffraction patterns of particles in the optical paths. Special sources of distortions are environmental distortions like vibrations and air turbulence.

All the aforementioned mentioned distortions affect the additive A and multiplicative B noise components:

$$|U_{Jn}| = A + B\left|J_n\left(\frac{4\pi}{\lambda}d_z - \phi_{BC}\right)\right|. \qquad (2.19)$$

The additional component A is eliminated due to phase-shifting. Within a detailed error analysis I have derived analytic formula:

$$dd_z = \frac{\lambda}{4\pi}\sqrt{\left[\left(sin2\dot{\Omega}^* dc_v\right)^2 + \left(sin2\dot{\Omega}^*\frac{\varepsilon}{4}d\varepsilon\right)^2 + \left(\frac{\partial\Delta(\Omega^*)}{\partial\Omega^*}d\Omega^*\right)^2\right]} \qquad (2.20)$$

providing better picture of how the individual disturbances contribute to overall error dd_z in amplitude distribution $d_z = \frac{\lambda}{4\pi}[\Omega^* + \Delta(\Omega^*)]$, where $\Delta(\Omega^*)$ is the correction function. The ratio $c_v = \frac{|\sigma(\tilde{B})|}{\tilde{B}_{AVE}}$ represents a coefficient of variation, while $\tilde{B}$ denotes distortions caused by drift of environmental conditions. In phase modulated holography there is in addition a contribution coming from phase offset error lying in interval ε.

Concretely four our experiment, the total error occurring in amplitude distribution as function of amplitude values is plotted in Figure 2.17.

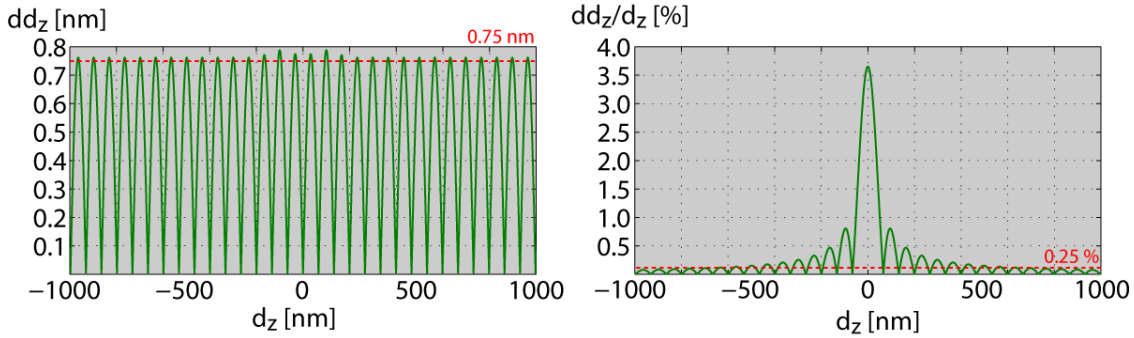

Figure 2.17: Error of measurement employing phase shifting technique as a function of measured amplitude of vibrations. Relative error is introduced in the right-hand plot.

Recently, error analysis has been largely replaced by uncertainty analysis. In order to convert error contributions into standard uncertainties, one has to estimate probability distribution of the individual distortion sources. Standard uncertainty

$$u_\varepsilon = \frac{\lambda\,\sigma^2(\varepsilon)}{32\pi} sin\left(\frac{8\pi}{\lambda} d_z\right) \tag{2.21}$$

represents uncertainty generated by incorrect phase offset. The second source of distortion considered within this analysis is the multiplicative factor $\tilde{B}$:

$$u_{\tilde{B}} = \frac{\lambda\sigma(\tilde{B})}{4\pi} sin\left(\frac{8\pi}{\lambda} d_z\right). \tag{2.22}$$

Analogously to error analysis, the third source of uncertainty is the correction function

$$u_\Delta = \frac{\partial\Delta(d_z)}{\partial d_z} dd_z. \tag{2.23}$$

Last considering source of distortion is repeatability (type A uncertainty while the above are all type B uncertainties) determined by relation (2.15):

$$u_A = 0.05 + 0.01\, d_z. \tag{2.24}$$

Formulas (2.21)-(2.24) can be used for definition of so called combined standard uncertainty:

$$u_c = \sqrt{{u_\varepsilon}^2 + {u_{\tilde{B}}}^2 + {u_\Delta}^2 + {u_A}^2} \tag{2.25}$$

comprising all important sources of distortions.
For illustration, combined standard uncertainties and expanded uncertainties (coverage factor $k = 2$) for some values of measured amplitude of vibrations d_z are presented in table below.

	$d_z = 10\ nm$	$d_z = 100\ nm$	$d_z = 1000\ nm$
$u_c\ [nm]$	0.4	1.3	10.1
$d_z \pm U\ (k = 2)$	$(10.0 \pm 0.8) nm$	$(100.0 \pm 2.6) nm$	$(1000.0 \pm 20.2) nm$

Another important parameter of measurement technique is its time consumption. In general, operators demand a quick and accurate measurement. The measurement time strongly depend on the employed hardware and software equipment (PC: intel core i5 3570 CPU, 8GB RAM). The driving of HW elements (Rigol DG 4102 waveform generators), acquisition (AVT Stingray camera: 6.5 FPS, 2048 x 2056 pixels) and data processing was performed in MATLAB R2013a environment via application built for this purpose. The measurement procedure consists of four steps:

- Initializing of the hardware (3.8 s)
- Capturing and saving of sequence of phase-shifted digital holograms at steady state of the object as a reference (1.4 s)

- Capturing and saving of phase-shifted digital holograms sequence at oscillating state with different phase-offsets (5.7 s)[9]
- Loading data and data processing (6.7 s)[1]

In total, the whole procedure takes less than 18s counted from the start of the measurement to visualization of distribution of vibration amplitudes over the whole surface.

3 Experiments

3.1 Measurement of piezoelectric transformers

A piezoelectric transformer (PT) is a device used for the transformation of alternating electric voltage by the means of ultrasonic vibrations. The measurement was performed for ring PTs and disc PTs with a different diameter and mounting. All piezoelectric transformers are made of hard lead zirconate titanate ceramics (PZT, APC841 type).
Firstly, the measured samples were ring PTs with a diameter of 40mm and thickness of 1mm. The electrodes were designed in the shape of concentric rings (similar to ring-dot design for the disk transformer). For the purpose of mounting, all transformers have a hole in the center and they are fixed onto a fitted shaft by the. For every mounted sample, its resonant frequencies were measured and then the holographic method for out-of-plane vibrations measurement was applied. The transformers were driven by voltages of 15, 30, 45, 60 V_{pp} and the out-of-plane displacement distributions near resonant frequencies were measured, data was processed and results were visualized by in-house developed applications. Some illustrative examples are introduced in Figure 3.1.

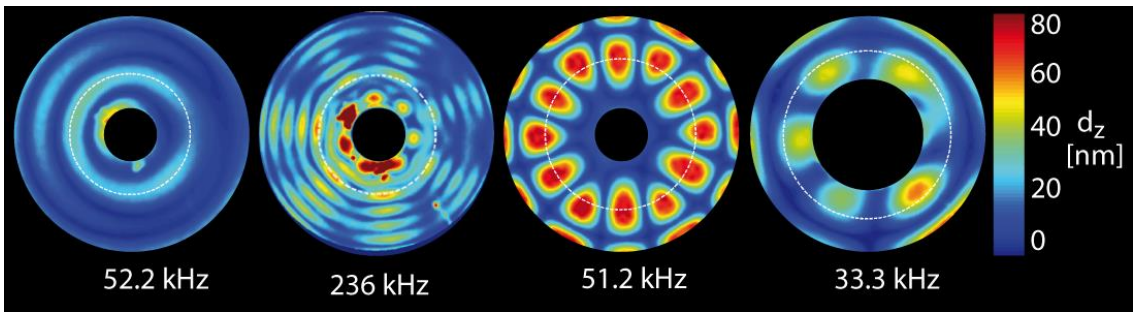

Figure 3.1: The out-of-plane displacement of ring piezoelectric transformer at resonant frequencies driven by $30V_{pp,}$ dashed white concentric circles represent the position of borderlines between electrode segments with diameters 8 mm and 20 mm.

The disc PTs have a 20mm diameter and a thickness of 1mm. Electrodes were designed in different shapes such as crescent-shaped, 2-, 3-, 4-segments PT, ring-dot or wedge V shape. The PTs were placed in a manufactured holder. The disc was pushed by a spring from the back-side to ensure that the pressure would be approximately identical

[9] Stands for 4-step phase shifting technique

during all measurements. The PTs were driven by a voltage of 30 V_{pp}. Some results of disc PT measurement are shown in Figure 3.2. The intensity of pseudo-color image corresponds to the amplitude of the vibration according to the color-bar on the right-hand side. The dark blue lines can be considered as nodal lines where the vibration amplitude is zero. Since the experiment was conducted without employment of phase modulation, only magnitude of oscillation amplitude is measured. The sign of mechanical phase is lost.

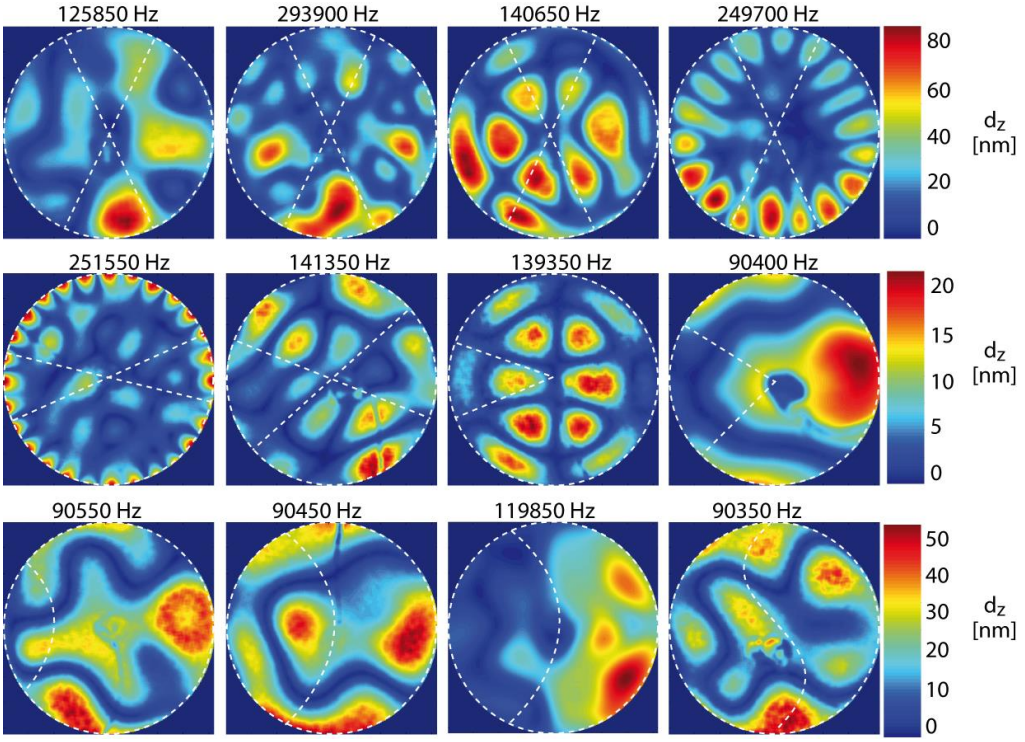

Figure 3.2: The out-of-plane displacement of disc piezoelectric transformers with differently shaped electrodes driven by $30V_{pp}$ at resonant frequencies. A diameter of a transformer is 20 mm and the dashed white lines represent position of borderlines between electrode segments.

Some additional study was performed on the PTs by infrared camera measurement and FEM Simulation.

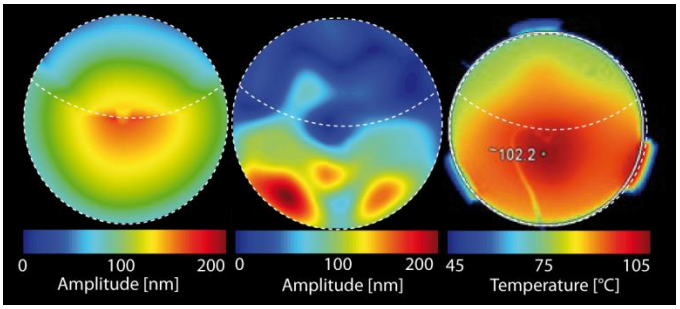

Figure 3.3: Investigation of disc PT by different techniques. Namely it is FEM simulation (left), holographic measurement (middle) and infrared camera visualization (right).

3.2 Comparison of frequency modulated technique to single point laser interferometer

Experiment introduced in this chapter shows the comparison of amplitude of vibration measurement simultaneously performed with three different methods on the same sample. The aim is to experimentally prove the capability of the frequency modulated time average digital holography combined with heterodyne technique and phase averaging. The methods used as a bench mark are Doppler vibrometry performed with commercial single point vibrometer and single point interferometer in Michelson construction which is improved with lock in principle. Figure 3.4 outlines the measurement arrangement. The vibrometer was precisely set to measure at the same point as the interferometric method. Since the holographic method measures in a whole-field, after the data evaluation, it was necessary to consider just the values, which correspond to single-point methods.

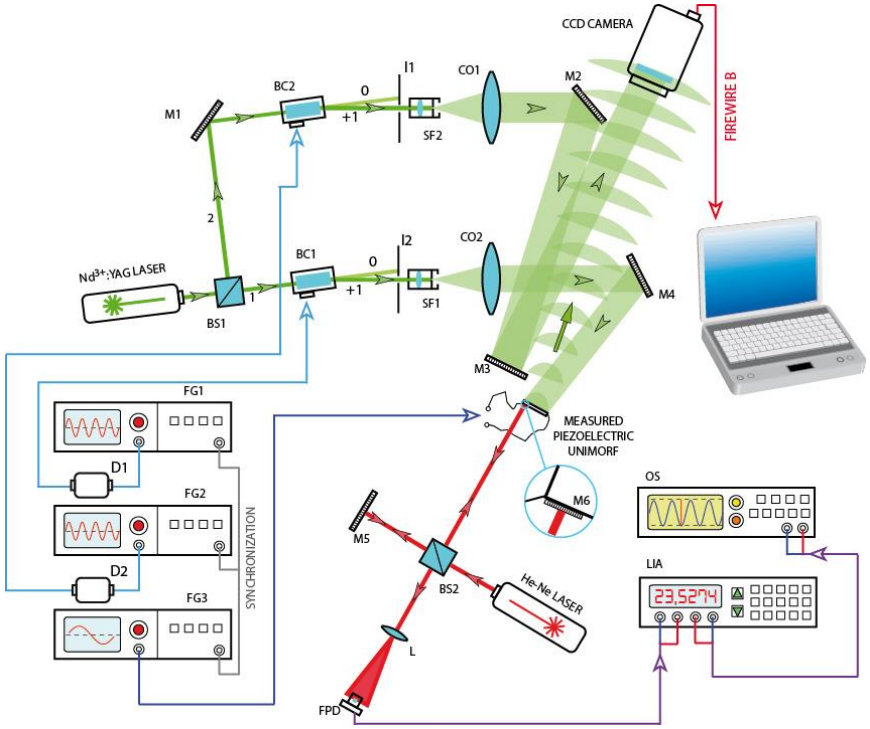

Figure 3.4: Holographic and interferometric arrangements for small amplitude vibration measurement.(BS-beam splitter, M-mirror, SF spatial filter, CO-collimating objective, O-focusing objective, FG-function generator, OS – oscillator, LIA – lock-in amplifier, L- lens, FPD – fast photodiode).

The object under investigation is piezoelectric unimorph membrane. The measurement was realized for three different driven frequencies: 2 khz, 9khz and 13 khz. For every frequency, set of measurement for different excitation voltages (10V, 20V, 30V, 50V, 100V, 200V) of the unimorph was performed. Due to thermal properties and relevance of measurements, the different method measurements were done in the same time. The interferometric lock-in method and the vibrometer based method are generally considered as a reliable and precise method and it was shown, the holographic method

has comparable parameters in the measurement range see Figure 3.5 - Figure 3.7. Some results obtained by the holographic method are presented in Figure 3.8.

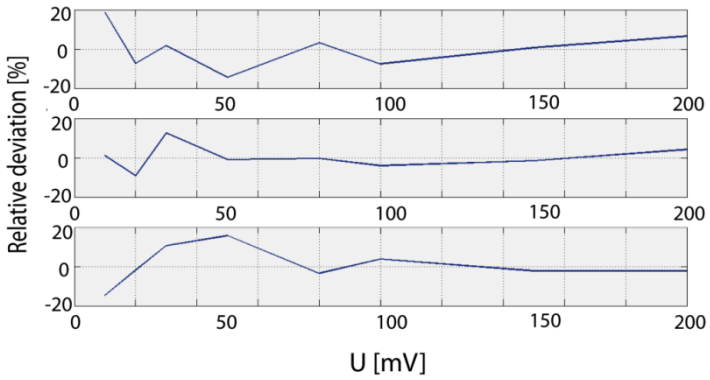

Figure 3.5: (up) Relative deviations between holographic and interferometric method (the average deviation is 7,513%); (middle) relative deviations between holographic and vibrometer method (the average deviation is 4,25%) and down - relative deviations between vibrometer and interferometric method (the average deviation is 6,85%);

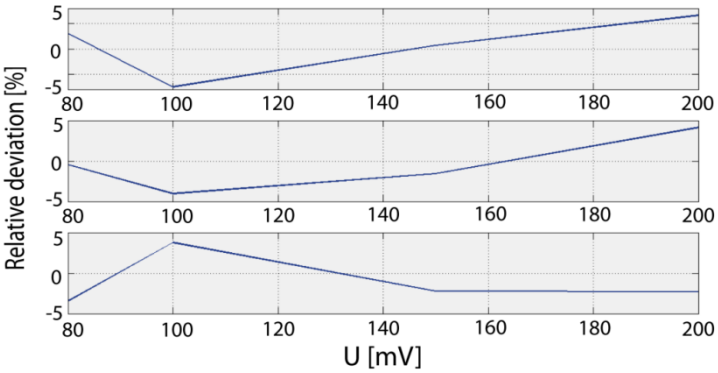

Figure 3.6: Relative deviations between methods (same ordering as in previous figure) for amplitudes larger than approximately 1nm with average deviation 4,47%, 2,54% and 2,93%.

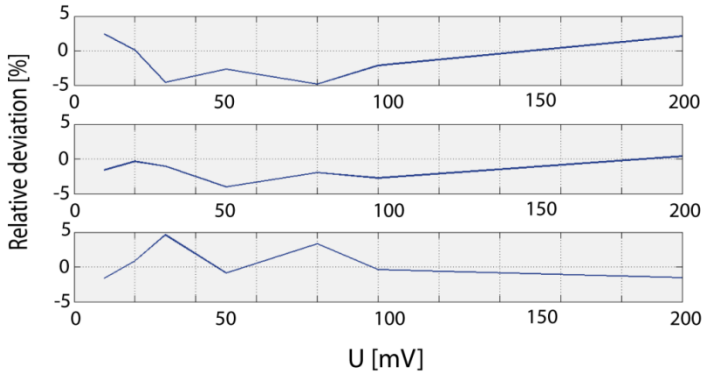

Figure 3.7: Up - relative deviations between holographic and interferometric method, middle - relative deviations between holographic and vibrometer method and down - relative deviations between vibrometer and interferometric method. The average deviation is smaller than 4%.

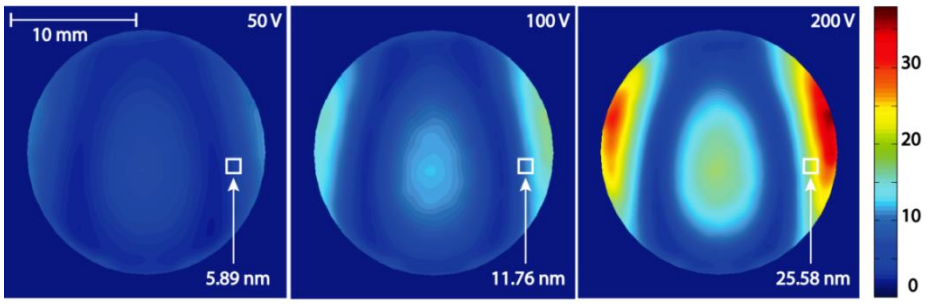

Figure 3.8: Results of piezoelectric unimorph measurement for driven frequency 2 kHz and excitation voltages 50V, 100V and 200V by digital holography. The white square denotes an area corresponding to the measuring area of the single point methods.

3.3 Noise suppression in curved glass shells using macro-fiber-composite actuators

This chapter introduces some experimental results of the semi-active control of noise transmission in a curved glass shell with attached piezoelectric macro fiber composite (MFC) actuators. The semi-active noise control is achieved via active elasticity control of piezoelectric actuators by connecting them to an active electric shunt circuit that has a negative effective capacitance. Using this approach, it is possible to suppress the vibration of the glass shell in the normal direction with respect to its surface and to increase the acoustic transmission loss of the piezoelectric MFC-glass composite structure. The effect of the MFC actuators connected to the negative capacitance shunt circuit on the surface distribution of the normal vibration amplitude is studied using phase and frequency modulated time average digital holography (PFMTADH).

The measurement of transmission loss by acoustic method was conducted at frequency range from 200 Hz to 800 Hz. Results are represented by solid green line in Figure 3.9. Subsequently, frequencies of 290 Hz and 735 Hz were identified with a minimum value of the acoustic transmission loss, which corresponds to dominant vibration modes of the curved glass shell. Finally, two values 270 Hz and 720 Hz of a frequency ω0 were chosen for which the NC was adjusted (marked by violet and blue circles).

The profiles of the vibration modes of the curved glass shell were measured using digital holography in the frequency ranges from 265 Hz to 275 Hz and from 715 Hz to 730 Hz in the two situations, when the NC was disconnected (OFF) and when the NC was connected and adjusted at the frequency 270 Hz, 720 Hz, respectively. Moreover, the NC was slightly detuned by capacity value in order to see the influence of this parameter. Figure 3.9 down shows the results. Values within each figure of amplitude distribution introduce rms value of the amplitudes over the whole surface.

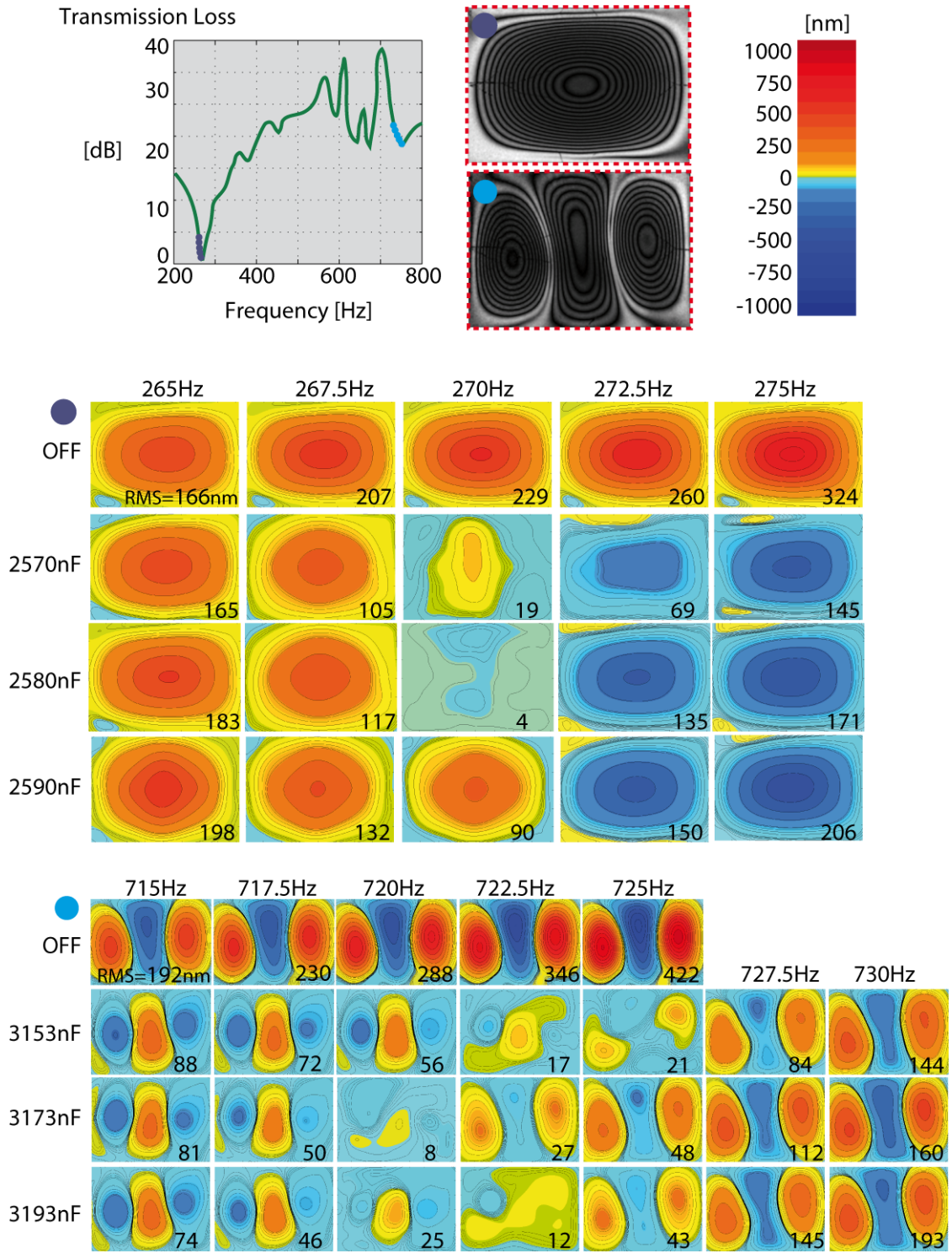

Figure 3.9: Results of experiments carried out on the glass shell with attached MFC for noise suppression. The 1D plot shows result of acoustic measurement. Magnitude maps of ROI measured at 270 Hz and 720 Hz by holographic method are introduced in the red dashed rectangles. The false color maps represent amplitudes of vibration within the ROI while the NC circuit is ON or OFF and for different values of capacity of the NC circuit. One should note that the colorbar is not linear due to large dynamic range of the measurement.

Conclusion

This dissertation is aimed to research and development of an advanced method for amplitudes of vibration measurement based on the digital holographic approach. The vibration analysis is massively used in many branches of industry as well as in research and development. The high demand for contactless, full-field and very sensitive method for vibration measurement combined with its complete lack let us to start with the method development. Although there is a vast amount of techniques for vibration analysis that are based on different principles, digital holography has offered new opportunities. Method for vibration measurement based on digital holography is called time-average digital holography (TADH). TADH is a whole-field method with great lateral resolution and unprecedented sensitivity. On the other hand, since its discovery, TADH has contended with drawbacks like a limited measurement range or lack of automatable quantitative analysis. The aim of this work was to push the limits of TADH and make the method easy-to-use and applicable in vast range of different applications. Based on previous research carried out in our research group I employed acusto-optical modulator (Bragg cell) into the experimental arrangement and combined advantages resulting from frequency and phase modulation of a reference or/and an object wave. The new method can be called phase and frequency modulated time average digital holography (PFMTADH). All theoretically derived impacts on the method caused by my inventions were experimentally verified by measurement of a beam cantilever.

The main results of the thesis can be summed up by following points:

- Different frequency modulation of the object and the reference wave in experimental arrangements results in temporally harmonic development of intensity values in digital hologram. This expresses relative phase variation between the both waves. In this way, arbitrary phase shift between frames of the digital sensor can be used for solution of set of equations by means of phase-shifting algorithms. As a result, one obtains wavefield in the **digital hologram** plane that **is free of undesired diffraction orders** called d.c. term or twin image. Thus bandwidth of the object in a digital hologram plane can be extended up to the bandwidth of the whole digital hologram. This leads to **improvement of the lateral resolution** within the surface of the object. Experiment shew the improvement of lateral resolution corresponding to the object surface about a factor of two when compared to single capture hologram. The object bandwidth covers more than 90% (in direction of maximal dimension of the object) of the total digital hologram bandwidth. These numbers are only indicative (stands only for this experiment), since lateral resolution in Fresnel holography depends on laser wavelength, parameters of used digital camera and distance between object and the camera.

- In addition, as a consequence of better lateral resolution, measurement range of the method in case of large amplitudes is increased. Better lateral resolution inevitable mitigates sampling criterion for the Bessel fringe pattern modulating the magnitude field over the object surface. Therefore larger amplitudes exhibiting denser fringe pattern can be resolved and evaluated.
- Due to combination of more digital holograms in phase-shifting technique, **signal-to-noise ratio is** also **increased** when compared to single captured digital hologram. The demonstrative experiment ascertained more energy within spectral domain of the object about 30%.
- When the reference wave is further modulated by an integer multiple of frequency at which the object oscillates, the order of the Bessel function defining the fringe pattern varies in connection with the integer value. Therefore one can easily make use of properties of different orders of the Bessel function. For very small amplitudes it is beneficial to modulate the reference wave by frequency of the object oscillations. This leads to first order Bessel function that exhibits sufficient slope for small values of vibration amplitudes.
- I experimentally established the threshold of the **smallest measurable amplitude to be under 0.1 nm**.
- In the case of large vibration amplitudes one can take advantage of the fact that the locations of the zeros of the Bessel functions are spread apart for increasing order of the Bessel function. Experimentally I reached **amplitude of vibration larger than 9 um** measured with modulation of reference wave by 150th multiple of the objet oscillations. It is worth noting that the dynamic range of the measurement has been increased due to frequency modulation up to 10000.
- In the next step I aimed at retrieval of vibrations amplitude values coded in the Bessel fringe pattern. I come up with method, where the Bragg cells employed in the holographic arrangements modulates phase of the reference wave. A sequence of phase modulated fringe patterns is reconstructed and with use of any of phase shifting algorithms the **amplitude of vibrations can be straightforwardly computed**. This procedure is elaborately introduced together with some experimental verification.
- **A repeatability** of the method was determined on the basis of experimental study to be **0.01 of measured amplitude** in nm plus bias 0.05 nm.
- I verified that frequency and phase modulation can be arbitrary combined in order to exploit benefits of the both approaches. **The dynamic range of 10000** was reached also with employment of the phase modulation.
- Further some sources of possible distortions influencing the accuracy of the method are discussed. A formula describing the total error of phase and frequency modulated is derived. Individual contributions to the total error are experimentally established and substitute into the error equation.

- Finally I determined the uncertainty of the method. As an example, **expanded uncertainty (k=2)** was calculated for nominal amplitude of vibrations 10 nm to be **(10.0 ± 0.8) nm** and **(1000.0 ± 20.2) nm** for nominal value 1000 nm. Obviously, analytical expression of the uncertainty for any nominal value is provided.
- **The developed techniques were applied** in some experiments. Measurement of disc and ring piezoelectric transformers evincing small amplitudes of vibration is introduced in chapter 4.1. Maps of vibration amplitudes over the transformers surface with differently shaped electrodes at resonant frequencies are measured and the results are used for further research in the field of piezoelectricity. **A reliability of the method was experimentally verified** by simultaneous measurement of a piezoelectric unimorph by three different techniques and results are presented in chapter 4.2. Namely it was laser interferometry with lock-in amplifier, commercial laser vibrometer and the developed holographic method. It was proofed that all the methods correspond in a range of 5 %. The developed method played a crucial role in an investigation of a semi-active noise control by active elasticity control of piezoelectric actuators. A characteristic feature of the measurement is its large dynamic range (when the control is on and off) and large number of performed measurements (different setting of the control circuit).

References

[1] R. A. Collacott, *Mechanical Vibrations: Their Calculation, Measurement, Effects and Suppression*. I. Pitman, 1947.

[2] K. G. McConnell and P. S. Varoto, *Vibration testing: theory and practice*. John Wiley & Sons, 1995.

[3] J. N. Butters and J. A. Leendertz, "Holographic and Video Techniques Applied to Engineering Measurement," *Measurement and Control*, vol. 4, no. 12, pp. 349–354, Dec. 1971.

[4] A. Macovski, S. D. Ramsey, and L. F. Schaefer, "Time-Lapse Interferometry and Contouring Using Television Systems," *Applied Optics*, vol. 10, no. 12, p. 2722, Dec. 1971.

[5] D. Gabor, "A new microscopic principle," *Nature*, vol. 161, no. 4098, pp. 777–778, 1948.

[6] E. N. Leith and J. Upatnieks, "Wavefront Reconstruction with Diffused Illumination and Three-Dimensional Objects," *Journal of the Optical Society of America*, vol. 54, no. 11, p. 1295, Nov. 1964.

[7] Y. N. Denisyuk, "Photographic Reconstruction of the Optical Properties of an Object in Its Own Scattered Radiation Field," *Soviet Physics Doklady*, vol. 7, p. 543, Dec. 1962.

[8] A. W. Lohmann and D. P. Paris, "Binary Fraunhofer Holograms, Generated by Computer," *Applied Optics*, vol. 6, no. 10, p. 1739, Oct. 1967.

[9] W.-H. Lee, "Binary Synthetic Holograms," *Applied Optics*, vol. 13, no. 7, p. 1677, Jul. 1974.

[10] W. H. Lee, "Sampled Fourier Transform Hologram Generated by Computer," *Applied Optics*, vol. 9, no. 3, p. 639, Mar. 1970.

[11] J. F. Heanue, M. C. Bashaw, and L. Hesselink, "Volume holographic storage and retrieval of digital data," *Science*, vol. 265, no. 5173, pp. 749–752, Aug. 1994.

[12] R. L. Powell and K. A. Stetson, "Interferometric Vibration Analysis by Wavefront Reconstruction," *Journal of the Optical Society of America*, vol. 55, no. 12, p. 1593, Dec. 1965.

[13] K. A. Stetson and R. L. Powell, "Interferometric Hologram Evaluation and Real-Time Vibration Analysis of Diffuse Objects," *Journal of the Optical Society of America*, vol. 55, no. 12, p. 1694, Dec. 1965.

[14] R. E. Brooks, L. O. Heflinger, and R. F. Wuerker, "INTERFEROMETRY WITH A HOLOGRAPHICALLY RECONSTRUCTED COMPARISON BEAM," *Applied Physics Letters*, vol. 7, no. 9, pp. 248–249, Nov. 1965.

[15] K. A. Haines and B. P. Hildebrand, "Surface-Deformation Measurement Using the Wavefront Reconstruction Technique," *Applied Optics*, vol. 5, no. 4, p. 595, Apr. 1966.

[16] B. P. Hildebrand and K. A. Haines, "The generation of three-dimensional contour maps by wavefront reconstruction," *Physics Letters*, vol. 21, no. 4, pp. 422–423, Jun. 1966.

[17] L. O. Heflinger and R. F. Wuerker, "Holographic Contouring via Multifrequency Lasers," *Applied Physics Letters*, vol. 15, pp. 28–30, Jul. 1969.

[18] M. H. Horman, "An Application of Wavefront Reconstruction to Interferometry," *Applied Optics*, vol. 4, no. 3, p. 333, Mar. 1965.

[19] D. W. Sweeney and C. M. Vest, "Reconstruction of Three-Dimensional Refractive Index Fields from Multidirectional Interferometric Data," *Applied Optics*, vol. 12, no. 11, p. 2649, Nov. 1973.

[20] I. H. Lira and C. M. Vest, "Refraction correction in holographic interferometry and tomography of transparent objects," *Applied optics*, vol. 26, no. 18, pp. 3919–3928, 1987.

[21] J. W. Goodman, "<title>Digital Image Formation From Electronically Detected Holograms</title>;," 1967, pp. 176–181.

[22] M.A. Kronrod, L.P. Yaroslavsky, and N.S. Merzlyakov, "Reconstruction of holograms with a computer," *Soviet Physics-Technical Physics*, vol. 17, no. 2, 1972.

[23] U. Schnars and W. Jüptner, "Direct recording of holograms by a CCD target and numerical reconstruction," *Applied Optics*, vol. 33, no. 2, p. 179, Jan. 1994.

[24] Y. Zou, G. Pedrini, and H. Tiziani, "Surface contouring in a video frame by changing the wavelength of a diode laser," *Opt. Eng*, vol. 35, no. 4, pp. 1074–1079, 1996.

[25] T. Kreis, *Handbook of holographic interferometry: optical and digital methods. 2005*. Weinheim: Wiley-VCH. xii.

[26] U. Schnars and W. Jueptner, *Digital holography: digital hologram recording, numerical reconstruction, and related techniques*. Springer, 2004.

[27] M. K. Kim, "Principles and techniques of digital holographic microscopy," *Journal of Photonics for Energy*, p. 018005, Apr. 2010.

[28] J. Garcia-Sucerquia, W. Xu, S. K. Jericho, P. Klages, M. H. Jericho, and H. J. Kreuzer, "Digital in-line holographic microscopy," *Applied optics*, vol. 45, no. 5, pp. 836–850, 2006.

[29] Y. Takaki and H. Ohzu, "Fast Numerical Reconstruction Technique for High-Resolution Hybrid Holographic Microscopy," *Applied Optics*, vol. 38, no. 11, p. 2204, Apr. 1999.

[30] F. Dubois, L. Joannes, and J.-C. Legros, "Improved Three-Dimensional Imaging with a Digital Holography Microscope With a Source of Partial Spatial Coherence," *Applied Optics*, vol. 38, no. 34, p. 7085, Dec. 1999.

[31] J. W. Goodman, "Temporal Filtering Properties of Holograms," *Applied Optics*, vol. 6, no. 5, p. 857, May 1967.

[32] C. C. Aleksoff, "Temporally modulated holography," *Applied Optics*, vol. 10, no. 6, pp. 1329–1341, 1971.

[33] M. Ueda, S. Miida, and T. Sato, "Signal-to-noise ratio and smallest detectable vibration amplitude in frequency-translated holography: an analysis," *Applied Optics*, vol. 15, no. 11, pp. 2690–2694, 1976.

[34] P. Picart, J. Leval, D. Mounier, and S. Gougeon, "Time-averaged digital holography," *Opt. Lett.*, vol. 28, no. 20, pp. 1900–1902, Oct. 2003.

[35] F. L. Clerc, L. Collot, and M. Gross, "Numerical heterodyne holography with two-dimensional photodetector arrays," *arXiv:1112.5080 [physics]*, Dec. 2011.

[36] F. Joud, F. Laloë, M. Atlan, J. Hare, and M. Gross, "Imaging a vibrating object by Sideband Digital Holography," *Optics Express*, vol. 17, no. 4, p. 2774, Feb. 2009.

[37] P. Psota, V. Ledl, R. Dolecek, J. Erhart, and V. Kopecky, "Measurement of piezoelectric transformer vibrations by digital holography," *IEEE Transactions on Ultrasonics, Ferroelectrics and Frequency Control*, vol. 59, no. 9, pp. 1962–1968, Sep. 2012.

[38] Lédl, P. Psota, R. Doleček, T. Vít, and J. Václavík, "Testing of a Recently Developed Digital Holographic Method for very Small Amplitude Measurements," 2013.

[39] N. Verrier and M. Atlan, "Absolute measurement of small-amplitude vibrations by time-averaged heterodyne holography with a dual local oscillator," *Opt Lett*, vol. 38, no. 5, pp. 739–741, Mar. 2013.

[40] D. N. Borza, "Mechanical vibration measurement by high-resolution time-averaged digital holography," *Measurement Science and Technology*, vol. 16, no. 9, p. 1853, 2005.

[41] C. S. Vikram, "A scheme for quantitative holographic vibration analysis from reconstructed irradiance data," *Journal of Modern Optics*, vol. 39, no. 10, pp. 1987–1989, 1992.

[42] P. Psota, V. Lédl, and R. Doleček, "High Dynamic Range Digital Holographic Method for Very Small Amplitude Measurement," in *Fringe 2013*, Springer, 2014, pp. 635–640.

[43] P. Psota, V. Lédl, R. Doleček, J. Václavík, and V. Kopeckỳ, "Improved holographic method for vibration amplitude measurement from nano to microscale," in *11TH INTERNATIONAL CONFERENCE ON VIBRATION MEASUREMENTS BY LASER AND NONCONTACT TECHNIQUES-AIVELA 2014: Advances and Applications*, 2014, vol. 1600, pp. 228–236.

[44] K. A. Stetson and W. R. Brohinsky, "Fringe-shifting technique for numerical analysis of time-average holograms of vibrating objects," *J. Opt. Soc. Am. A*, vol. 5, no. 9, pp. 1472–1476, Sep. 1988.

[45] P. Psota, V. Lédl, P. Vojtíšek, J. Václavík, R. Doleček, and P. Mokrý, "Advanced time average holographic method for measurement in extensive vibration amplitude range with quantitative single-pixel analysis," 2015, vol. 9508, p. 95080N–95080N–9.

[46] J. Erhart, P. Pulpan, R. Dolecek, P. Psota, and V. Ledl, "Disc piezoelectric ceramic transformers," *Ultrasonics, Ferroelectrics, and Frequency Control, IEEE Transactions on*, vol. 60, no. 8, pp. 1612–1618, 2013.

[47] J. Erhart, P. Pulpan, R. Dolecek, P. Psota, and V. Ledl, "Disc piezoelectric ceramic transformers," in *Applications of Ferroelectrics held jointly with 2012 European Conference on the Applications of Polar Dielectrics and 2012 International Symp Piezoresponse Force Microscopy and Nanoscale Phenomena in Polar Materials (ISAF/ECAPD/PFM), 2012 Intl Symp*, 2012, pp. 1–4.

[48] V. Lédl, P. Psota, R. Dolecek, J. Erhart, and V. Kopecky, "A digital holographic method for the measurement of piezoelectric transformer vibrations," in *Applications of Ferroelectrics (ISAF/PFM), 2011 International Symposium on and 2011 International Symposium on Piezoresponse Force Microscopy and Nanoscale Phenomena in Polar Materials*, 2011, pp. 1–4.

[49] P. Psota, V. Kopeckỳ, V. Lédl, and R. Doleček, "Digital Holographic Method for Piezoelectric Transformers Vibration Analysis," *EPJ Web of Conferences*, vol. 48, p. 00021, 2013.

[50] P. Psota, V. Kopecky, R. Dolecek, and V. Ledl, "Digital Holographic Method for Piezoelectric Transformers Vibration Analysis," in *Optics and Measurement International Conference Proceedings*, Liberec, 2012.

[51] P. Mokrý, P. Psota, K. Steiger, J. Václavík, R. Doleček, V. Lédl, and M. Šulc, "Noise suppression in curved glass shells using macro-fiber-composite actuators studied by the means of digital holography and acoustic measurements," *AIP Advances*, vol. 5, no. 2, p. 027132, Feb. 2015.

[52] P. MOKRÝ, K. Steiger, J. Vaclavik, P. Psota, R. DOLECEK, P. Marton, M. KODEJŠKA, and others, "Noise shielding using active acoustic metamaterials with electronically tunable acoustic impedance."

[53] K. Novakova, P. Psota, R. Dolecek, V. Ledl, P. Mokry, J. Vaclavik, P. Marton, and M. Cernik, "Planar acoustic metamaterials with the active control of acoustic impedance using a piezoelectric composite actuator," in *Applications of Ferroelectric and Workshop on the Piezoresponse Force Microscopy (ISAF/PFM), 2013 IEEE International Symposium on the*, 2013, pp. 317–320.

[54] P. Mokrý, K. Steiger, J. Václavík, P. Psota, R. Doleček, P. Márton, M. Kodejška, and M. Černík, "Noise shielding using active acoustic metamaterials with electronically tunable acoustic impedance," in *INTERNOISE2014 Proceedings*, Melbourne, AUSTRALIA, 2014, pp. 1–9.

[55] P. Psota, V. Ledl, R. Dolecek, P. Mokry, and V. Kopecky, "Measurement of vibration mode structure for adaptive vibration suppression system by digital holography," in *Applications of Ferroelectric and Workshop on the Piezoresponse Force Microscopy (ISAF/PFM), 2013 IEEE International Symposium on the*, 2013, pp. 214–217.

Author's list of publications

[1] P. Psota, V. Lédl, P. Vojtíšek, R. Doleček, and and P. Mokrỳ, "Advanced time average holographic method for measurement in extensive vibration amplitude range with quantitative single-pixel analysis," in SPIE Optics+ Optoelectronics, 2015, p. 95080N–95080N. *(1st place – Best Student Paper Award)*

[2] P. Psota, V. Lédl, P. Vojtíšek, R. Doleček, and V. Kopeckỳ, "3D form inspection of grinded optical surfaces by digital holography," in Optics and Measurement Conference 2014, 2015, pp. 944218–944218. *(2nd place – Best Student Paper Award)*

[3] P. Mokrỳ, P. Psota, K. Steiger, J. Václavík, R. Doleček, V. Lédl, and M. Šulc, "Noise suppression in curved glass shells using macro-fiber-composite actuators studied by the means of digital holography and acoustic measurements," AIP Advances, vol. 5, no. 2, p. 027132, 2015.

[4] P. Mokry, K. Steiger, P. Psota, R. Dolecek, P. Vojtisek, and V. Ledl, "Digital holographic interferometry as an experimental instrumentation for measurements of macroscopic properties of polydomain ferroelectrics," in Optics and Measurement Conference 2014, 2015, p. 94420V–94420V.

[5] V. Lédl, P. Psota, P. Vojtíšek, R. Doleček, P. Mokrỳ, and M. Dlask, "Challenges in holographic measurement of aspheric and freeform optical components shape," in SPIE Optics+ Optoelectronics, 2015, p. 95080M–95080M.

[6] V. Lédl, P. Psota, P. Vojtíšek, R. Doleček, and P. Mokrỳ, "Holographic contouring and its limitations in nearly specularly reflecting surface measurement," in Optics and Measurement Conference 2014, 2015, p. 94420Q–94420Q.

[7] V. Lédl, P. Psota, R. Doleček, and T. Vít, "Digital holographic setups for phase object measurements in micro and macro scale," EPJ Web of Conferences, vol. 92, p. 01001, 2015.

[8] R. Doleček, P. Psota, V. Lédl, T. Vít, P. Dančová, and V. Kopeckỳ, "Comparison of digital holographic interferometry and constant temperature anemometry for measurement of temperature field in fluid," in SPIE Optics+ Optoelectronics, 2015, p. 95080P–95080P.

[9] P. Psota, V. Lédl, R. Doleček, J. Václavík, and V. Kopeckỳ, "Improved holographic method for vibration amplitude measurement from nano to microscale," in 11TH INTERNATIONAL CONFERENCE ON VIBRATION MEASUREMENTS BY LASER AND NONCONTACT TECHNIQUES-AIVELA 2014: Advances and Applications, 2014, vol. 1600, pp. 228–236.

[10] P. Psota, V. Lédl, and R. Doleček, "High Dynamic Range Digital Holographic Method for Very Small Amplitude Measurement," in Fringe 2013, Springer, 2014, pp. 635–640.

[11] V. Lédl, P. Psota, T. Vít, and R. Doleček, "Digital Holographic Setup for Measurement of Fast Developing Phenomenon in Wide Area," in Fringe 2013, Springer, 2014, pp. 577–580.

[12] R. Doleček, P. Psota, V. Lédl, T. Vít, and V. Kopeckỳ, "Comparison of holographic setups used in heat and mass transfer measurement," EPJ Web of Conferences, vol. 67, p. 02021, 2014.

[13] T. Vít, V. Lédl, R. Dolecek, and P. Psota, "The Possibility of Visualizing Temperature Fields Using Digital Holographic Interferometry," in Applied Mechanics and Materials, 2013, vol. 284, pp. 988–995.

[14] J. Vaclavík, R. Doleček, V. Lédl, and P. Psota, "Experimental study on SPDT machining of Gallium Phosphide," in SPIE Optifab, 2013, p. 88842H–88842H.

[15] P. Psota, V. Ledl, R. Dolecek, P. Mokry, and V. Kopecky, "Measurement of vibration mode structure for

adaptive vibration suppression system by digital holography," in Applications of Ferroelectric and Workshop on the Piezoresponse Force Microscopy (ISAF/PFM), 2013 IEEE International Symposium on the, 2013, pp. 214–217.

[16] P. Psota, V. Ledl, R. Dolecek, and V. Kopecky, "Holographic Nano-scale Amplitude Measurement Method with Expanded Dynamic Range," in Digital Holography and Three-Dimensional Imaging, 2013, p. DTh5A–1.

[17] P. Psota, V. Kopeckỳ, V. Lédl, and R. Doleček, "Digital Holographic Method for Piezoelectric Transformers Vibration Analysis," EPJ Web of Conferences, vol. 48, p. 00021, 2013.

[18] K. Novakova, P. Psota, R. Dolecek, V. Ledl, P. Mokry, J. Vaclavik, P. Marton, and M. Cernik, "Planar acoustic metamaterials with the active control of acoustic impedance using a piezoelectric composite actuator," in Applications of Ferroelectric and Workshop on the Piezoresponse Force Microscopy (ISAF/PFM), 2013 IEEE International Symposium on the, 2013, pp. 317–320.

[19] R. Melich, P. Psota, V. Lédl, and J. Václavík, "Irregular surfaces-measurements and ZEMAX simulations," EPJ Web of Conferences, vol. 48, p. 00015, 2013.

[20] V. Lédl, P. Psota, J. Václavík, R. Doleček, and P. Vojtíšek, "Multiwavelength digital holography for polishing tool shape measurement," in SPIE Optifab, 2013, p. 88840E–88840E.

[21] J. Erhart, P. Pulpan, R. Dolecek, P. Psota, and V. Ledl, "Disc piezoelectric ceramic transformers," Ultrasonics, Ferroelectrics, and Frequency Control, IEEE Transactions on, vol. 60, no. 8, pp. 1612–1618, 2013.

[22] R. Doleček, P. Psota, V. Lédl, T. Vít, J. Václavík, and V. Kopeckỳ, "General temperature field measurement by digital holography," Applied optics, vol. 52, no. 1, pp. A319–A325, 2013.

[23] R. Doleček, V. Kopeckỳ, P. Psota, and V. Lédl, "Digital Holographic setup for Measurement of Asymmetric Temperature Field and Tomographic Reconstruction," EPJ Web of Conferences, vol. 48, p. 00003, 2013.

[24] P. Psota, V. Lédl, R. Doleček, J. Václavík, and M. Šulc, "Comparison of digital holographic method for very small amplitudes measurement with single point laser interferometer and laser doppler vibrometer," in Digital Holography and Three-Dimensional Imaging, 2012, p. DSu5B–3.

[25] P. Psota, V. Ledl, R. Dolecek, J. Erhart, and V. Kopecky, "Measurement of piezoelectric transformer vibrations by digital holography," Ultrasonics, Ferroelectrics, and Frequency Control, IEEE Transactions on, vol. 59, no. 9, pp. 1962–1968, 2012.

[26] V. Lédl, T. Vít, R. Doleček, and P. Psota, "Digital holografic interferometry used for identification of 2D temperature field," EPJ Web of Conferences, vol. 25, p. 02014, 2012.

[27] R. Doleček, P. Psota, V. Lédl, T. Vít, J. Václavík, and V. Kopeckỳ, "Measurement of Asymmetric Temperature Field by Using Digital Holographic Multidirectional Interferometry," in Digital Holography and Three-Dimensional Imaging, 2012, p. DSu5B–2.

[28] P. Dancova, T. Vit, Z. Travnicek, V. Ledl, and P. Psota, "Methods of measurement of the temperature field in pulsatile fluid," ICHMT DIGITAL LIBRARY ONLINE, 2012.

[29] P. Psota, V. Lédl, P. Vojtíšek, Device to measure shape of optical surfaces, especially diffusion-reflective surfaces, Utility model nr. 27893

[30] V. Lédl, P. Psota, P. Vojtíšek, and J. Křížek, Expanded measurement range interefometer, Utility model nr. 27615